

Temporally-Similar Structure-Aware Spatiotemporal Fusion of Satellite Images

Ryosuke Isono *Student Member, IEEE*, Shunsuke Ono, *Member, IEEE*,

Abstract—This paper proposes a novel spatiotemporal (ST) fusion framework for satellite images, named Temporally-Similar Structure-Aware ST fusion (TSSTF). ST fusion is a promising approach to address the trade-off between the spatial and temporal resolution of satellite images. In real-world scenarios, observed satellite images are severely degraded by noise due to measurement equipment and environmental conditions. Consequently, some recent studies have focused on enhancing the robustness of ST fusion methods against noise. However, existing noise-robust ST fusion approaches often fail to capture fine spatial structure, leading to oversmoothing and artifacts. To address this issue, TSSTF introduces two key mechanisms: Temporally-Guided Total Variation (TGTV) and Temporally-Guided Edge Constraint (TGEC). TGTV is a novel regularization function that promotes spatial piecewise smoothness while preserving structural details, guided by a reference high spatial resolution image acquired on a nearby date. TGEC enforces consistency in edge locations between two temporally adjacent images, while allowing for spectral variations. We formulate the ST fusion task as a constrained optimization problem incorporating TGTV and TGEC, and develop an efficient algorithm based on a pre-conditioned primal-dual splitting method. Experimental results demonstrate that TSSTF performs comparably to state-of-the-art methods under noise-free conditions and outperforms them under noisy conditions. Additionally, we provide a comprehensive set of recommended parameter values that consistently yield high performance across diverse target regions and noise conditions, aiming to enhance reproducibility and practical utility.

Index Terms—Spatiotemporal fusion, remote sensing, total variation, constrained optimization, primal-dual splitting method

I. INTRODUCTION

THE analysis of temporal image series is necessary and important in many remote sensing applications, such as vegetation/crop monitoring and estimation [1], evapotranspiration estimation [2], atmosphere monitoring [3], land-cover/land-use change detection [4], surface dynamic mapping [5], ecosystem monitoring [6], soil water content analysis [7], and detailed analysis of human-nature interactions [8]. These applications require time series of high spatial resolution images to properly model the ground surface. In addition, time series of high temporal resolution images are also needed to capture the changes in the ground surface that occur over short periods of time.

However, there is a trade-off between the temporal and spatial resolution of satellite sensors, and no single sensor can satisfy both requirements. For example, the Landsat sensors can acquire images with a high spatial resolution of 30-m, but they have a revisit period of up to 16 dates. On the other hand, the Moderate resolution Imaging Spectroradiometer (MODIS) sensors can acquire images for the same scene at least once per date, but the images are at a low spatial resolution of 500-m [9]. Therefore, the simultaneous acquisition of image series of high spatial and high temporal resolution is a major challenge in the remote sensing community [10]. The direct solution to this challenge is simply to estimate an unobserved high spatial resolution (HR) image from the single corresponding low spatial resolution (LR) image by super-resolution [11], [12]. However, this is too difficult because the spatial resolution gap between the two satellite images is often quite large.

Spatiotemporal fusion (ST fusion) addresses this challenge by leveraging HR and LR image pairs acquired on reference dates that are temporally close to the target date. Specifically, the unobserved HR image on the target date is estimated by integrating the spatial structure extracted from the reference HR images and the spectral changes inferred from the two temporally adjacent LR images.

In ideal situations where reliable reference images are available, accurate ST fusion would be easy to achieve because the correct spatial structure and spectral changes are readily available. However, in real-world applications, such situations are very rare. This is because satellite images are often contaminated with various types of noise including random noise, outliers, and missing values [13], [14], due to the measurement equipment and/or environmental conditions. ST fusion methods that do not account for such noise would produce noisy target HR images, which will have a significant negative impact on subsequent processing. Therefore, from a practical point of view, it is crucial to develop a noise-robust ST fusion method.

A. Prior Research

ST fusion has been extensively studied over the past decades. From a methodological perspective, existing ST fusion techniques can be broadly classified into three groups: rule-based, learning-based, and optimization-based approaches. Rule-based methods estimate the target HR image using explicitly defined rules, such as weighted averaging or spectral unmixing [9], [15]–[19]. They are the most traditional and have laid the foundation for subsequent developments in this field. Recently, learning-based methods have been

R. Isono is with the Department of Computer Science, Institute of Science Tokyo, Yokohama, 226-8503, Japan (e-mail: isono.r.1f44@m.isct.ac.jp).

S. Ono is with the Department of Computer Science, Institute of Science Tokyo, Yokohama, 226-8503, Japan (e-mail: ono@comp.isct.ac.jp).

This work was supported in part by JST FOREST under Grant JPMJFR232M, JST AdCORP under Grant JPMJKB2307, JST ACT-X under Grant JPMJAX24C1, and JST BOOST under Grant JPMJBS2430, and in part by JSPS KAKENHI under Grant 22H03610, 22H00512, 23H01415, 23K17461, 24K03119, 24K22291, 25H01296, and 25K03136.

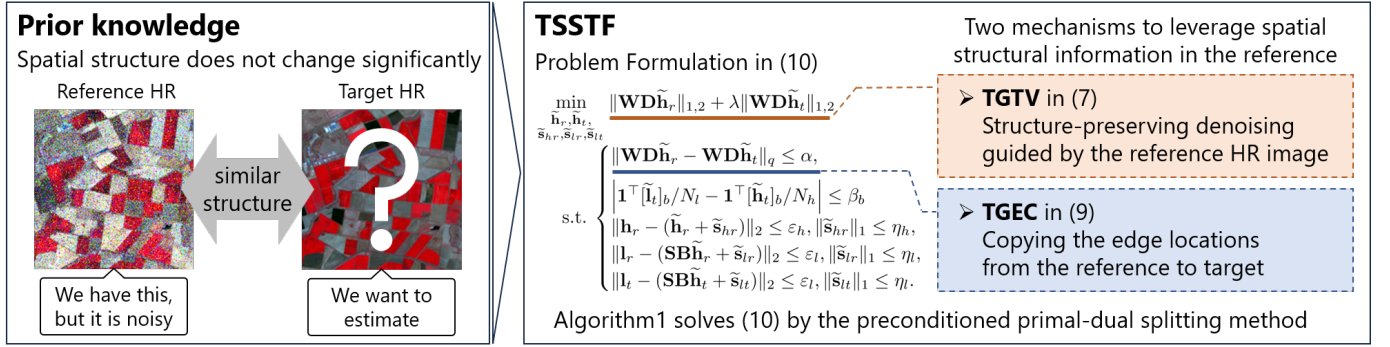


Fig. 1. Illustration of our TSSTF.

proposed by leveraging machine learning models to learn a direct mapping from observed HR-LR pairs to the target HR image [20]–[27]. By utilizing a large amount of extra training data, these methods are effective at capturing complex land cover structure and nonlinear temporal variations without explicitly modeling them. In contrast, optimization-based methods formulate the ST fusion task as an optimization problem and solve it either analytically or using optimization algorithms [28]–[32]. A key advantage of these methods is that they do not require any external training data; instead, they rely solely on the observed HR and LR images to perform the fusion in a self-contained and model-driven manner.

Although a wide variety of ST fusion methods have been proposed, most are designed without explicitly accounting for noise. Consequently, they may fail in real-world scenarios where measurement noise is inevitable. To the best of our knowledge, only two methods have been developed with a specific focus on robustness to noise: a learning-based method called robust spatiotemporal fusion network (RSFN) [24], and an optimization-based method called robust optimization-based spatiotemporal fusion (ROSTF) [30].

RSFN mitigates the impact of noise by employing convolutional neural networks (CNNs), generative adversarial networks (GANs), and an attention mechanism. It takes as input two reference HR-LR image pairs acquired before and after the target date, along with a LR image on the target date. The attention mechanism is designed to suppress the influence of noisy pixels. Specifically, it compares the two reference HR images and places greater reliance on the less noisy one in each spatial region. However, this strategy can be effective only when the noisy pixels do not appear at the same locations across the two references. In practice, this assumption rarely holds because noise often affects entire images. Moreover, RSFN assumes that the noise follows a Gaussian distribution, limiting its applicability to other noise types commonly observed in satellite data. Additionally, the requirement for future observations does not align with the fundamental goal of ST fusion, which aims to estimate the HR image at the target date using only currently available or earlier observations.

To achieve more practical ST fusion, ROSTF was developed to handle mixed Gaussian and sparse noise affecting the entire image, requiring only a single past HR-LR image pair as

well as a LR image on the target date. It introduces an observation model that explicitly characterizes how such noise contaminates satellite images. By incorporating this observation model along with prior knowledge of temporal satellite image series, ROSTF formulates ST fusion and noise removal as a unified optimization problem. This formulation allows the two tasks to be performed simultaneously, enabling noise-robust ST fusion suitable for real-world scenarios. However, a significant limitation still remains: the loss of original spatial structure. The noise removal process in ROSTF relies on total variation (TV) regularization [33]–[35], a widely used technique in image denoising. While TV effectively promotes piecewise-smoothness in the estimated image, this regularization operates independently of the intrinsic spatial structure in the underlying noise-free image. Consequently, it cannot distinguish between noise and meaningful fine structure, such as edges, that should be preserved. As a result, ROSTF tends to oversmooth the image and introduce unnatural artifacts, degrading spatial fidelity.

B. Contributions and Paper Organization

Now, a natural question arises: *Is it possible to achieve noise-robust ST fusion while preserving the original spatial structure?* To answer this question, we propose a new ST fusion framework called Temporally-Similar Structure-Aware ST fusion (TSSTF). When the reference and target dates are temporally close, the corresponding HR images are expected to have similar spatial structure. Exploiting this prior knowledge, TSSTF accurately extracts the underlying spatial structure from the noisy reference image and effectively reflects it to the estimated target HR image. The TSSTF framework is built upon the following two key mechanisms as illustrated in Fig. 1.

- **Temporally-Guided Total Variation:** We develop a novel regularization function specialized for ST fusion, termed temporally-guided total variation (TGTV), which effectively captures the spatial characteristics of the reference HR image. TGTV evaluates neighborhood differences with adaptive weights derived from the reference HR image, unlike standard total variation, which treats them all uniformly. Minimizing TGTV promotes spatial piecewise-smoothness while preserving the original spatial structure.

- *Temporally-Guided Edge Constraint*: When the reference and target HR images share similar spatial structure, the locations of their edges are likely to coincide. On the other hand, the edge intensities may vary due to temporal changes in the spectral brightness of the surrounding regions. Then, we develop a constraint, termed the temporally-guided edge constraint (TGEC), that enforces the consistency of edge locations while allowing for variations in edge intensities.

By incorporating these mechanisms, we formulate ST fusion as a constrained optimization problem. Specifically, the objective function consists of TGTV, while the constraints include TGEC along with data-fidelity conditions. To solve this problem, we construct an efficient algorithm based on a preconditioned primal-dual splitting method (P-PDS) [36]. This approach can automatically determine the appropriate stepsizes for solving the optimization problem.

The main contributions of this paper are given as follows.

- 1) *Improved Robustness to Noise*: Existing robust ST fusion methods suffer from limitations such as over-smoothing and artifact generation. In this paper, we address this issue by introducing two temporally-similar structure-aware mechanisms: TGTV and TGEC. TGTV is a novel regularization function that promotes piecewise-smoothness while preserving edges by exploiting the spatial structure in the reference HR image. TGEC is a novel constraint to copy only the edge locations—not their intensities—from the reference HR image to the estimated target HR image. By integrating these two mechanisms into a unified optimization framework, we achieve improved robustness in ST fusion while faithfully preserving the original spatial structure.
- 2) *Facilitation of Parameter Adjustment*: The objective function of the TSSTF optimization problem consists only of TGTV for image regularization, while other components are incorporated as hard constraints. Such a formulation using constraints instead of adding terms to the objective function offers the advantage of simplifying parameter setting [37]–[41]: the parameters associated with each constraint are independent of each other and can be adjusted separately. Furthermore, our experiments show that each parameter can be set semi-automatically based on prior information.
- 3) *Automatic Stepsize Adjustment*: To efficiently solve our optimization problem, we develop an algorithm based on P-PDS with an operator-norm-based design method of variable-wise diagonal preconditioning technique (OVDP) [42]. The appropriate stepsizes of the standard PDS [43] (and most other optimization methods) would be different depending on the problem structure, which means that we have to select them manually. On the other hand, P-PDS with OVDP can automatically determine the appropriate stepsizes based on the problem structure, thus freeing our algorithm from such a troublesome task.

In the following sections, we first cover the mathematical preliminaries for our method in Sec. II and then move on to

the establishment of our method in Sec. III. In Sec. IV, we demonstrate the performance of TSSTF through comparative experiments. Experimental results show that TSSTF performs comparably to several state-of-the-art ST fusion methods for noiseless images and better than them for noisy images. Additionally, we provide a recommended set of parameters for TSSTF, which can be determined based on prior information.

The preliminary version of this work, without considering sparse noise, mathematical details, comprehensive experimental comparison, deeper discussion, has appeared in conference proceedings [44].

II. PRELIMINARIES

A. Notations

Let \mathbb{R} be the set of all real numbers. Vectors and matrices are denoted by bold lower and upper case letters, respectively. We represent a multispectral image with spatial resolution $W \times H$ and B spectral bands as a vector $\mathbf{x} \in \mathbb{R}^{WHB}$, where $x_{i,j,b}$ denotes the pixel value at the location (i, j) in the b -th spectral band. Let $\Gamma_0(\mathbb{R}^{WHB})$ be the set of all proper lower-semicontinuous convex functions defined on \mathbb{R}^{WHB} . The ℓ_1 -norm, the ℓ_2 -norm, and the mixed $\ell_{1,2}$ -norm of \mathbf{x} are defined as $\|\mathbf{x}\|_1 := \sum_{i,j,b} |x_{i,j,b}|$, $\|\mathbf{x}\|_2 := \sqrt{\sum_{i,j,b} |x_{i,j,b}|^2}$, and $\|\mathbf{x}\|_{1,2} := \sum_{i,j} \sqrt{\sum_b |x_{i,j,b}|^2}$, respectively. For an image $\mathbf{x} \in \mathbb{R}^{WHB}$, let $\mathbf{D}_1, \mathbf{D}_2, \mathbf{D}_3$, and $\mathbf{D}_4 \in \mathbb{R}^{WHB \times WHB}$ denote the matrices for computing the differences between each pixel value and its four neighborhood pixel values as follows:

$$\begin{aligned} [\mathbf{D}_1 \mathbf{x}]_{i,j,b} &= x_{i+1,j,b} - x_{i,j,b}, [\mathbf{D}_2 \mathbf{x}]_{i,j,b} = x_{i+1,j-1,b} - x_{i,j,b}, \\ [\mathbf{D}_3 \mathbf{x}]_{i,j,b} &= x_{i,j-1,b} - x_{i,j,b}, [\mathbf{D}_4 \mathbf{x}]_{i,j,b} = x_{i-1,j-1,b} - x_{i,j,b}. \end{aligned}$$

Then, let $\mathbf{D} := (\mathbf{D}_1^\top \mathbf{D}_2^\top \mathbf{D}_3^\top \mathbf{D}_4^\top)^\top \in \mathbb{R}^{4WHB \times WHB}$. The hyperslab with the center ω and radius α is denoted as

$$S_\alpha^\omega := \{\mathbf{z} | |\omega - \mathbf{1}^\top \mathbf{z}| \leq \alpha\}.$$

The norm ball with the center \mathbf{c} and radius ε is denoted as

$$B_q^{\mathbf{c},\varepsilon} := \{\mathbf{z} | \|\mathbf{z} - \mathbf{c}\|_q \leq \varepsilon\},$$

for the ℓ_1 -norm, ℓ_2 -norm, and mixed $\ell_{1,2}$ -norm. The indicator function $\iota_C : \mathbb{R}^N \rightarrow (-\infty, \infty]$ of a nonempty closed convex set C is defined as

$$\iota_C := \begin{cases} 0, & \text{if } \mathbf{x} \in C, \\ \infty, & \text{otherwise.} \end{cases} \quad (1)$$

B. Proximal Tools

The optimization problem of TSSTF that will be formulated in Sec. III-E consists of nonsmooth convex functions. To solve such a problem, we introduce the notion of the *proximal operator* of index $\gamma > 0$ of $f \in \Gamma_0(\mathbb{R}^{WHB})$ as follows:

$$\text{prox}_{\gamma f} : \mathbb{R}^{WHB} \rightarrow \mathbb{R}^{WHB} : \mathbf{x} \mapsto \argmin_{\mathbf{y} \in \mathbb{R}^{WHB}} f(\mathbf{y}) + \frac{1}{2\gamma} \|\mathbf{x} - \mathbf{y}\|_2^2.$$

The Fenchell-Rockefeller conjugate function f^* of the function $f \in \Gamma_0(\mathbb{R}^{WHB})$ is denoted by

$$f^*(\mathbf{y}) := \sup_{\mathbf{x} \in \mathbb{R}^{WHB}} \{\langle \mathbf{x}, \mathbf{y} \rangle - f(\mathbf{x})\}.$$

Thanks to Moreus's identity [45], the proximity operator of f^* is efficiently calculated as

$$\text{prox}_{\gamma f^*}(\mathbf{x}) = \mathbf{x} - \gamma \text{prox}_{\frac{1}{\gamma} f}(\frac{1}{\gamma} \mathbf{x}).$$

Below, we show the specific proximity operators of the functions that we use in this paper. The proximity operator of the mixed $\ell_{1,2}$ -norm is given by

$$[\text{prox}_{\gamma \|\cdot\|_{1,2}}(\mathbf{x})]_{i,j,b} = \max \left\{ 1 - \frac{\gamma}{\sqrt{\sum_{b'=1}^B |x_{i,j,b'}|^2}}, 0 \right\} x_{i,j,b}.$$

The proximity operator of the indicator function ι_C is equivalent to the projection onto the set C , given by

$$\text{prox}_{\gamma \iota_C}(\mathbf{x}) = P_C(\mathbf{x}) := \underset{\mathbf{y} \in C}{\text{argmin}} \|\mathbf{x} - \mathbf{y}\|_2.$$

The projection onto the hyperslab is expressed as follows:

$$P_{S_\alpha^\omega}(\mathbf{x}) = \begin{cases} \mathbf{x} + \frac{\eta_1 - 1}{WHB} \mathbf{x}, & \text{if } \mathbf{1}^\top \mathbf{x} < \eta_1, \\ \mathbf{x} + \frac{\eta_2 - 1}{WHB} \mathbf{x}, & \text{if } \mathbf{1}^\top \mathbf{x} > \eta_2, \\ \mathbf{x}, & \text{otherwise,} \end{cases}$$

where $\eta_1 = \omega - \alpha$ and $\eta_2 = \omega + \alpha$. The projections onto the ℓ_2 -norm ball and the ℓ_1 -norm ball are calculated by

$$P_{B_2^{c,\varepsilon}}(\mathbf{x}) = \begin{cases} \mathbf{x}, & \text{if } \mathbf{x} \in \iota_{B_2^{c,\varepsilon}}, \\ \mathbf{c} + \frac{\varepsilon(\mathbf{x}-\mathbf{c})}{\|\mathbf{x}-\mathbf{c}\|_2}, & \text{otherwise,} \end{cases}$$

and a fast ℓ_1 -ball projection algorithm [46], respectively. The projection onto the mixed $\ell_{1,2}$ -norm ball with the center $\mathbf{0} \in \mathbb{R}^{HWB}$ is calculated by

$$[P_{B_{1,2}^{0,\varepsilon}}(\mathbf{x})]_{i,j} = \begin{cases} \mathbf{0} \in \mathbb{R}^B, & \text{if } \|\mathbf{x}\|_{i,j} = 0, \\ \zeta_{i,j} \frac{[\mathbf{x}]_{i,j}}{\|\mathbf{x}\|_{i,j}}, & \text{otherwise,} \end{cases}$$

where $[\mathbf{x}]_{i,j} = (x_{i,j,1}, \dots, x_{i,j,B}) \in \mathbb{R}^B$ and $\zeta = P_{B_1^{0,\varepsilon}}(\|\mathbf{x}\|_{1,1}, \dots, \|\mathbf{x}\|_{W,H}) \in \mathbb{R}^{WH}$.

C. P-PDS with OVDP

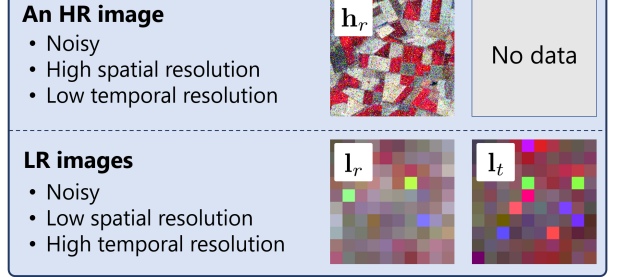
The standard PDS [43] is a versatile and efficient proximal algorithm that can solve a wide class of nonsmooth convex optimization problems without using matrix inversion. However, it is troublesome to manually set the appropriate stepsizes of the standard PDS. Therefore, we adopt P-PDS [36] with OVDP [42], a method that automatically determines the appropriate stepsizes according to the problem structure.

Let $\mathbf{y}_i \in \mathbb{R}^{K_i}$ ($i = 1, \dots, N$) and $\mathbf{z}_j \in \mathbb{R}^{L_j}$ ($j = 1, \dots, M$). Consider convex optimization problems of the following form:

$$\begin{aligned} \min_{\mathbf{y}_1, \dots, \mathbf{y}_N, \mathbf{z}_1, \dots, \mathbf{z}_M} & \sum_{i=1}^N g_i(\mathbf{y}_i) + \sum_{j=1}^M h_j(\mathbf{z}_j), \\ \text{s.t. } & \mathbf{z}_j = \sum_{i=1}^N \mathbf{G}_{j,i} \mathbf{y}_i, \quad \forall j \in \{1, \dots, M\}, \end{aligned} \quad (2)$$

where $g_i \in \Gamma_0(\mathbb{R}^{K_i})$ ($i = 1, \dots, N$), $h_j \in \Gamma_0(\mathbb{R}^{L_j})$ ($j = 1, \dots, M$), and $\mathbf{G}_{j,i} : \mathbb{R}^{K_i} \rightarrow \mathbb{R}^{L_j}$ ($i = 1, \dots, N$, $j =$

Input



Output

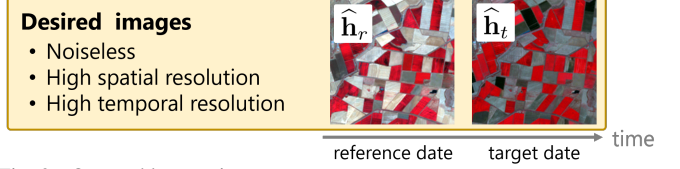


Fig. 2. Our problem setting

$1, \dots, M$) are linear operators. P-PDS with OVDP solves (2) by the following iterative procedures:

```

for  $i = 1, \dots, N$  do
     $\bar{\mathbf{y}}_i^{(n)} \leftarrow \mathbf{y}_i^{(n)} - \gamma_{1,i} \sum_{j=1}^M \mathbf{G}_{j,i}^\top \mathbf{z}_j^{(n)}$ ,
     $\mathbf{y}_i^{(n+1)} \leftarrow \text{prox}_{\gamma_{1,i} g_i}(\bar{\mathbf{y}}_i^{(n)})$ ,
end for
for  $j = 1, \dots, M$  do
     $\bar{\mathbf{z}}_j^{(n)} \leftarrow \mathbf{z}_j^{(n)} + \gamma_{2,j} \sum_{i=1}^N \mathbf{G}_{j,i} (2\mathbf{y}_i^{(n+1)} - \mathbf{y}_i^{(n)})$ ,
     $\mathbf{z}_j^{(n+1)} \leftarrow \text{prox}_{\gamma_{2,j} h_j}(\bar{\mathbf{z}}_j^{(n)})$ ,
end for

```

where $\gamma_{1,i}$ ($i = 1, \dots, N$) and $\gamma_{2,j}$ ($j = 1, \dots, M$) are step-size parameters. The stepsize parameters can be determined automatically as follows [42]:

$$\gamma_{1,i} = \frac{1}{\sum_{j=1}^M \|\mathbf{G}_{j,i}\|_{\text{op}}^2}, \quad \gamma_{2,j} = \frac{1}{N},$$

where $\|\cdot\|_{\text{op}}$ is the operator norm defined by

$$\|\mathbf{G}\|_{\text{op}} := \sup_{\mathbf{x} \neq \mathbf{0}} \frac{\|\mathbf{G}\mathbf{x}\|_2}{\|\mathbf{x}\|_2}.$$

III. PROPOSED METHOD

In this section, we first organize the problem setting and introduce the observation models for high-resolution (HR) and low-resolution (LR) images. Then, we establish two main mechanisms, temporally-guided total variation (TGTv) and temporally-guided edge constraint (TGEC). After that, we formulate our optimization problem based on these mechanisms and develop an algorithm to solve it.

A. Problem Setting

In this paper, we consider a practical scenario where a single HR-LR image pair acquired on a past reference date

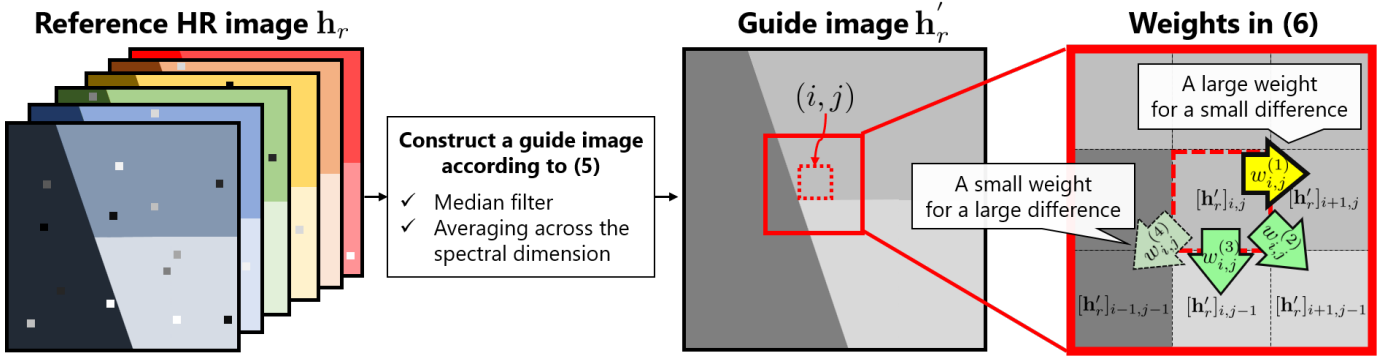


Fig. 3. Illustration of the weights in (6). A noise-attenuated guide image \mathbf{h}_r' in (5) is first constructed from the reference HR image. The weights are then computed from this guide image according to (6). In the right panel, each arrow corresponds to a weight; the darker the arrow, the greater the weight.

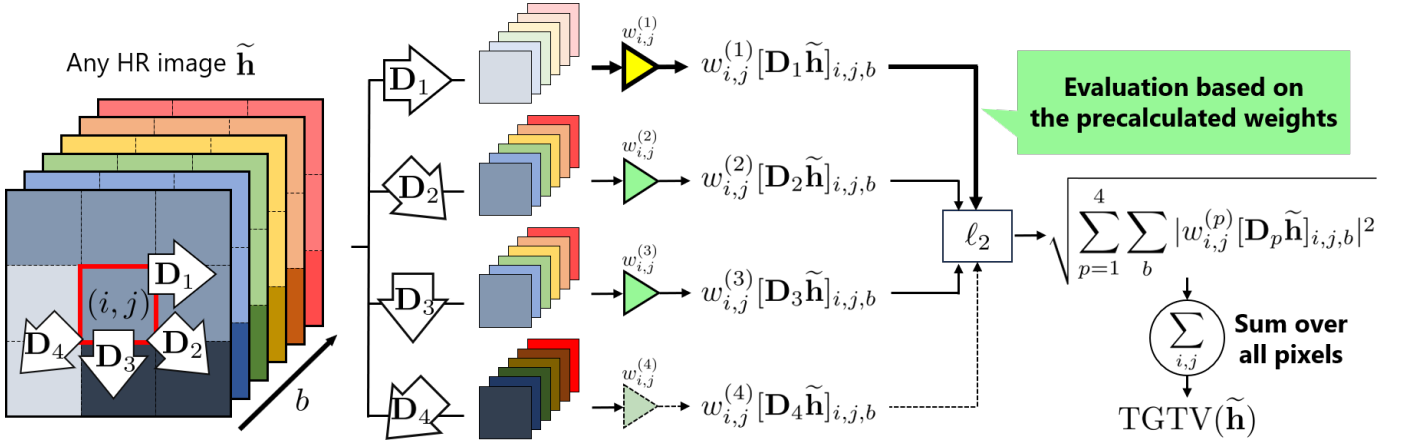


Fig. 4. Illustration of TGTv. TGTv evaluates the four neighborhood differences with adaptive weights derived from the guided HR image \mathbf{h}_r' .

is available, together with an LR image acquired on the target date. This setting is realistic because the availability of multiple HR-LR pairs is often limited in real-world applications due to various factors such as cloud contamination, temporal inconsistency in image acquisition, or limited data accessibility. Therefore, ST fusion methods that require only a single reference HR-LR pair are applicable to a wider range of real-world cases than those requiring multiple reference pairs, although such a situation is obviously challenging [47].

Let the HR image on the reference date, and the LR image on the reference date, and the LR image on the target date be $\mathbf{h}_r \in \mathbb{R}^{W_h H_h B}$, $\mathbf{l}_r \in \mathbb{R}^{W_l H_l B}$, and $\mathbf{l}_t \in \mathbb{R}^{W_l H_l B}$, respectively. As shown in Fig. 2, our goal is to estimate $\hat{\mathbf{h}}_t \in \mathbb{R}^{W_h H_h B}$ (the noiseless HR image on the target date) based on these three observed images, while simultaneously denoising \mathbf{h}_r , i.e., estimating $\hat{\mathbf{h}}_r$ (the noiseless HR image on the reference date). For simplicity of description, we use $N_h := W_h H_h$ and $N_l := W_l H_l$ as needed.

B. Observation Models

Let $\hat{\mathbf{h}} \in \mathbb{R}^{N_h B}$ and $\hat{\mathbf{l}} \in \mathbb{R}^{N_l B}$ be a noiseless HR image and a noiseless LR image, respectively, taken on the same date. We introduce observation models for a noisy HR image $\mathbf{h} \in \mathbb{R}^{N_h B}$ and a noisy LR image $\mathbf{l} \in \mathbb{R}^{N_l B}$. Specifically, we consider that the observed satellite images \mathbf{h} and \mathbf{l} are possibly contaminated

with random noise, outliers, and missing values. Random noise added to $\hat{\mathbf{h}}$ and $\hat{\mathbf{l}}$ is modeled by Gaussian noise \mathbf{n}_h and \mathbf{n}_l with standard deviation σ_h and σ_l , respectively, while outliers and missing values affecting $\hat{\mathbf{h}}$ and $\hat{\mathbf{l}}$ are modeled by sparsely distributed noise \mathbf{s}_h and \mathbf{s}_l with the superimposition ratio r_h and r_l , respectively. By modeling the noise in this manner, the observation models for \mathbf{h} and \mathbf{l} are described as

$$\begin{aligned} \mathbf{h} &= \hat{\mathbf{h}} + \mathbf{n}_h + \mathbf{s}_h, \\ \mathbf{l} &= \hat{\mathbf{l}} + \mathbf{n}_l + \mathbf{s}_l. \end{aligned} \quad (3)$$

Here, $\sigma_h > \sigma_l$ and $r_h > r_l$ generally hold since HR images often contain more severe noise than LR images. This is because the amount of light received per pixel decreases as the number of pixels increases [48].

On the other hand, $\hat{\mathbf{l}}$ can be approximated by the image obtained by blurring and down-sampling $\hat{\mathbf{h}}$, known as a typical super-resolution model [49], as follows:

$$\hat{\mathbf{l}} = \mathbf{S}\mathbf{B}\hat{\mathbf{h}} + \mathbf{m}, \quad (4)$$

where $\mathbf{B} \in \mathbb{R}^{N_h B \times N_h B}$ is the spatial spread transform matrix introduced in [50], $\mathbf{S} \in \mathbb{R}^{N_l B \times N_h B}$ is the down-sampling matrix, and $\mathbf{m} \in \mathbb{R}^{N_l B}$ is the modeling error. This model has been widely used in the ST fusion literature [51].

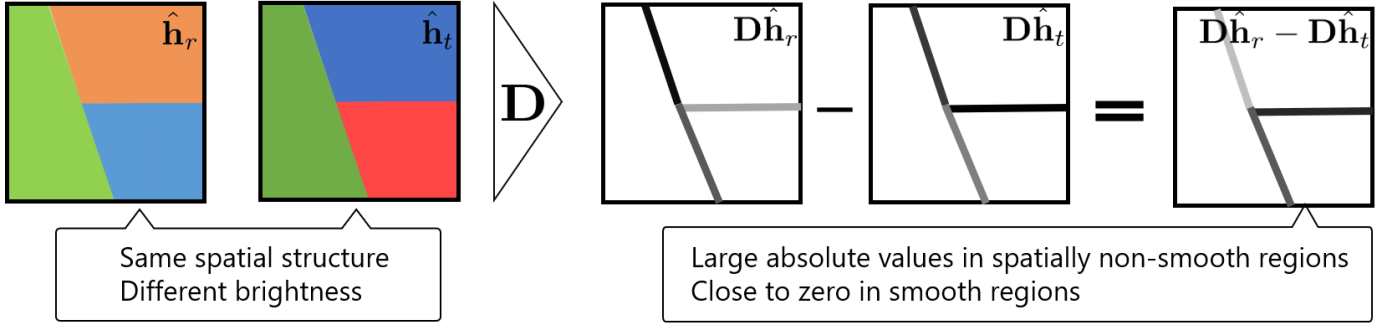


Fig. 5. Illustration of edge similarity. When the reference and target dates are temporally close, the locations of edges are likely to coincide. On the other hand, edge intensities may differ due to changes in the spectral brightness of surrounding regions over time.

C. Temporally-Guided Total Variation

To achieve simultaneous denoising and ST fusion, we introduce a regularization function imposed on the HR images. Total variation (TV) regularization is widely used for denoising, due to its ability to promote piecewise smoothness [33], [34]. However, standard TV regularization does not explicitly account for the underlying spatial structure in the image, which can result in over-smoothing. To overcome this limitation, we propose a novel regularization function that effectively captures the spatial structure of the target region by leveraging a reference HR image \mathbf{h}_r .

In practical scenarios, \mathbf{h}_r is often contaminated by noise, which hinders accurate extraction of spatial structure. Therefore, we construct a guide image $\mathbf{h}'_r \in \mathbb{R}^{N_h}$ as follows:

$$\mathbf{h}'_r := \frac{1}{B} \sum_{b=1}^B \text{Med}([\mathbf{h}_r]_b), \quad (5)$$

where $[\mathbf{h}_r]_b \in \mathbb{R}^{N_h}$ denotes the b -th spectral band of \mathbf{h}_r . Specifically, we first apply a median filter $\text{Med}(\cdot) : \mathbb{R}^{N_h} \rightarrow \mathbb{R}^{N_h}$ to each spectral band of \mathbf{h}_r to suppress noise, especially sparse outliers and missing values. The filtered bands are then averaged across the spectral dimension to yield a grayscale guide image. This guide image preserves the dominant spatial structure of \mathbf{h}_r while effectively reducing random noise.

Based on the guide image \mathbf{h}'_r , we define a weight $w_{i,j}^{(p)}$ for each pixel location (i, j) and direction $p \in 1, 2, 3, 4$ as follows:

$$w_{i,j}^{(p)} = \exp\left(-\frac{1}{\delta^2} |[\mathbf{D}_p \mathbf{h}'_r]_{i,j}|^2\right), \quad (6)$$

where δ is a parameter controlling the sensitivity of the weights to spatial differences. As shown in Fig. 3, this formulation assigns larger weights to directions where the local difference in \mathbf{h}'_r is small, and smaller weights where the difference is large, thereby reflecting the underlying spatial structure. To further enhance structural selectivity, we introduce an additional parameter $k \in 1, 2, 3, 4$, and set to zero the k smallest values among $w_{i,j}^{(1)}, w_{i,j}^{(2)}, w_{i,j}^{(3)}, w_{i,j}^{(4)}$ for each (i, j) . This operation effectively suppresses the influence of directions with minimal structural similarity.

For each direction p , we arrange the weights $\{w_{i,j}^{(p)}\}$ diagonally to make $\mathbf{W}^{(p)} := \text{diag}(w_{1,1}^{(p)}, \dots, w_{W_h, H_h}^{(p)}) \in \mathbb{R}^{N_h \times N_h}$, and then replicate $\mathbf{W}^{(p)}$ across the spectral bands to form $\bar{\mathbf{W}}^{(p)} := \text{diag}(\mathbf{W}^{(p)}, \dots, \mathbf{W}^{(p)}) \in \mathbb{R}^{N_h B \times N_h B}$. Finally, the

overall weight matrix \mathbf{W} is defined by stacking the four matrices $\bar{\mathbf{W}}^{(p)}$ as follows:

$$\mathbf{W} := \text{diag}(\bar{\mathbf{W}}^{(1)}, \bar{\mathbf{W}}^{(2)}, \bar{\mathbf{W}}^{(3)}, \bar{\mathbf{W}}^{(4)}) \in \mathbb{R}^{4N_h B \times 4N_h B}.$$

Using this weight matrix, we define our proposed regularization function, temporally-guided total variation (TGTV), for any HR image $\tilde{\mathbf{h}} \in \mathbb{R}^{N_h B}$ as follows:

$$\text{TGTV}(\tilde{\mathbf{h}}) := \|\mathbf{W} \mathbf{D} \tilde{\mathbf{h}}\|_{1,2} = \sum_{i,j} \sqrt{\sum_b \sum_{p=1}^4 |w_{i,j}^{(p)} [\mathbf{D}_p \tilde{\mathbf{h}}]_{i,j,b}|^2}. \quad (7)$$

As shown in Fig. 4, TGTV evaluates the four neighborhood differences with adaptive weights derived from the guided image \mathbf{h}'_r . Therefore, minimizing TGTV encourages the estimated image to exhibit spatial smoothness in regions where the guided image \mathbf{h}'_r is homogeneous, while preserving edges and structural discontinuities where \mathbf{h}'_r exhibits strong spatial differences. As a result, TGTV promotes piecewise smoothness while preserving the intrinsic spatial structure.

D. Temporally-Guided Edge Constraint

When the reference and target dates are temporally close, the corresponding HR images are expected to share similar spatial structure, which means that the locations of edges are likely to coincide. Based on this prior knowledge, we propose a novel constraint that enforces the edges in the reference and target HR images to appear at the same spatial locations.

A simple way to incorporate this prior knowledge is to directly compare the edge intensities of the two images and constrain their difference to be small. This can be expressed as the following constraint:

$$\|\mathbf{D} \tilde{\mathbf{h}}_r - \mathbf{D} \tilde{\mathbf{h}}_t\|_q \leq \alpha, \quad (8)$$

where $\tilde{\mathbf{h}}_r$ and $\tilde{\mathbf{h}}_t$ denote the estimated reference and target HR images, respectively, q indicates the norm used to measure the difference, and α is a small positive constant that controls the allowable discrepancy.

While this constraint has been shown to copy edges from the reference HR image to the target HR image [30], it suffers from a critical limitation: it does not account for temporal variations in edge intensities between the two images. Such intensity variations are caused by changes in the spectral

brightness of surrounding regions over time. Consequently, the components of $\mathbf{D}\tilde{\mathbf{h}}_r - \mathbf{D}\tilde{\mathbf{h}}_t$ tend to have large absolute values in spatially non-smooth regions, while they are close to zero in spatially smooth regions, as illustrated in Fig. 5. Nevertheless, the constraint in (8) evaluates all components of $\mathbf{D}\tilde{\mathbf{h}}_r - \mathbf{D}\tilde{\mathbf{h}}_t$ equally, enforcing them to approach zero uniformly, which can introduce undesired artifacts.

To address this issue, we incorporate the same weighting scheme used in TGTv as follows:

$$\|\mathbf{W}(\mathbf{D}\tilde{\mathbf{h}}_r - \mathbf{D}\tilde{\mathbf{h}}_t)\|_q \leq \alpha. \quad (9)$$

The matrix \mathbf{W} assigns larger weights to smooth regions and smaller values to non-smooth regions based on the guide image \mathbf{h}'_r as defined in (6). Thus, this constraint encourages the components of $\mathbf{D}\tilde{\mathbf{h}}_r - \mathbf{D}\tilde{\mathbf{h}}_t$ to approach zero preferentially in smooth regions, while allowing flexibility in non-smooth regions. As a result, the constraint can tolerate temporal variations in edge intensities while still enforcing consistency in the edge locations. We refer to the constraint as the temporally-guided edge constraint (TGEC) because it is guided by the weight matrix \mathbf{W} derived from the temporally adjacent HR image.

Regarding the choice of the norm q in TGEC, we evaluated several candidates, including the ℓ_1 norm, the ℓ_2 norm, and the mixed $\ell_{1,2}$ norm. Among them, the mixed $\ell_{1,2}$ norm was found to yield the best performance in our experiments. For detailed comparisons, please refer to Sec. IV-E3.

E. Problem Formulation

Based on the TGTv and TGEC mechanisms, we formulate the ST fusion task as the following constrained optimization problem:

$$\begin{aligned} \min_{\substack{\tilde{\mathbf{h}}_r, \tilde{\mathbf{h}}_t, \\ \tilde{\mathbf{s}}_{hr}, \tilde{\mathbf{s}}_{lr}, \tilde{\mathbf{s}}_{lt}}} \quad & \|\mathbf{W}\mathbf{D}\tilde{\mathbf{h}}_r\|_{1,2} + \lambda \|\mathbf{W}\mathbf{D}\tilde{\mathbf{h}}_t\|_{1,2} \\ \text{s.t.} \quad & \begin{cases} \|\mathbf{W}\mathbf{D}\tilde{\mathbf{h}}_r - \mathbf{W}\mathbf{D}\tilde{\mathbf{h}}_t\|_q \leq \alpha, \\ \left| \mathbf{1}^\top [\tilde{\mathbf{l}}_t]_b / N_l - \mathbf{1}^\top [\tilde{\mathbf{l}}_r]_b / N_h \right| \leq \beta_b \quad (b = 1, \dots, B), \\ \|\mathbf{h}_r - (\tilde{\mathbf{h}}_r + \tilde{\mathbf{s}}_{hr})\|_2 \leq \varepsilon_h, \\ \|\mathbf{l}_r - (\mathbf{S}\mathbf{B}\tilde{\mathbf{h}}_r + \tilde{\mathbf{s}}_{lr})\|_2 \leq \varepsilon_l, \\ \|\mathbf{l}_t - (\mathbf{S}\mathbf{B}\tilde{\mathbf{h}}_t + \tilde{\mathbf{s}}_{lt})\|_2 \leq \varepsilon_l, \\ \|\tilde{\mathbf{s}}_{hr}\|_1 \leq \eta_h, \\ \|\tilde{\mathbf{s}}_{lr}\|_1 \leq \eta_l, \\ \|\tilde{\mathbf{s}}_{lt}\|_1 \leq \eta_l, \end{cases} \end{aligned} \quad (10)$$

where λ is a balancing parameter. The variables $\tilde{\mathbf{h}}_r$ and $\tilde{\mathbf{h}}_t$ correspond to the estimates of $\hat{\mathbf{h}}_r$ and $\hat{\mathbf{h}}_t$, respectively, and $\tilde{\mathbf{s}}_{hr}$, $\tilde{\mathbf{s}}_{lr}$ and $\tilde{\mathbf{s}}_{lt}$ correspond to the estimates of sparse noise superimposed on \mathbf{h}_r , \mathbf{l}_r and \mathbf{l}_t , respectively. Each term in the objective function and each constraint have the following roles.

- The two terms in the objective function are TGTv, which promote spatial piecewise smoothness of $\tilde{\mathbf{h}}_r$ and $\tilde{\mathbf{h}}_t$, while preserving the original spatial structure.
- The first constraint is TGEC, which encourages the edges in the reference and target HR images to appear at the same spatial locations.

- The second constraint ensures that the target HR and LR images have similar average spectral brightness per band [30]. This holds when the HR and LR sensors have the same spectral resolution, which is a common assumption in the context of ST fusion.
- The third to fifth constraints serve as data-fidelity based on the observation models in (3) and (4).
- The last three constraints characterize the sparse noise using the ℓ_1 -norms.

Using constraints instead of adding terms to the objective function in this way simplifies the parameter setting [37]–[41]: we can determine the appropriate parameters for each constraint independently because they are decoupled. The detailed setting of these parameters is discussed in Sec. IV-B.

F. Optimization

For solving (10) by an algorithm based on P-PDS with OVDp, we need to transform (10) into the form of (2). First, using the indicator function (see (1) for the definition), we reformulate our problem in (10) as follows:

$$\begin{aligned} \min_{\substack{\tilde{\mathbf{h}}_r, \tilde{\mathbf{h}}_t, \\ \tilde{\mathbf{s}}_{hr}, \tilde{\mathbf{s}}_{lr}, \tilde{\mathbf{s}}_{lt}}} \quad & \|\mathbf{W}\mathbf{D}\tilde{\mathbf{h}}_r\|_{1,2} + \lambda \|\mathbf{W}\mathbf{D}\tilde{\mathbf{h}}_t\|_{1,2} \\ & + \iota_{B_q^{0,\alpha}}(\mathbf{W}\mathbf{D}\tilde{\mathbf{h}}_r - \mathbf{W}\mathbf{D}\tilde{\mathbf{h}}_t) \\ & + \sum_{b=1}^B \iota_{S^{N_h \mathbf{1}^\top [\tilde{\mathbf{l}}_t]_b / N_l}}([\tilde{\mathbf{h}}_t]_b) + \iota_{B_2^{\mathbf{h}_r, \varepsilon_h}}(\tilde{\mathbf{h}}_r + \tilde{\mathbf{s}}_{hr}) \\ & + \iota_{B_2^{\mathbf{l}_r, \varepsilon_l}}(\mathbf{S}\mathbf{B}\tilde{\mathbf{h}}_r + \tilde{\mathbf{s}}_{lr}) + \iota_{B_2^{\mathbf{l}_t, \varepsilon_l}}(\mathbf{S}\mathbf{B}\tilde{\mathbf{h}}_t + \tilde{\mathbf{s}}_{lt}) \\ & + \iota_{B_1^{0,\eta_h}}(\tilde{\mathbf{s}}_{hr}) + \iota_{B_1^{0,\eta_l}}(\tilde{\mathbf{s}}_{lr}) + \iota_{B_1^{0,\eta_l}}(\tilde{\mathbf{s}}_{lt}). \end{aligned} \quad (11)$$

Introducing auxiliary variables \mathbf{z}_1 , \mathbf{z}_2 , \mathbf{z}_3 , \mathbf{z}_4 , \mathbf{z}_5 , and \mathbf{z}_6 , we can transform (11) into the following equivalent problem:

$$\begin{aligned} \min_{\substack{\tilde{\mathbf{h}}_r, \tilde{\mathbf{h}}_t, \\ \tilde{\mathbf{s}}_{hr}, \tilde{\mathbf{s}}_{lr}, \tilde{\mathbf{s}}_{lt}}} \quad & \|\mathbf{z}_1\|_{1,2} + \lambda \|\mathbf{z}_2\|_{1,2} + \sum_{b=1}^B \iota_{S^{N_h \mathbf{1}^\top [\tilde{\mathbf{l}}_t]_b / N_l}}([\tilde{\mathbf{h}}_t]_b) \\ & + \iota_{B_q^{0,\alpha}}(\mathbf{z}_3) + \iota_{B_2^{\mathbf{h}_r, \varepsilon_h}}(\mathbf{z}_4) + \iota_{B_2^{\mathbf{l}_r, \varepsilon_l}}(\mathbf{z}_5) + \iota_{B_2^{\mathbf{l}_t, \varepsilon_l}}(\mathbf{z}_6) \\ & + \iota_{B_1^{0,\eta_h}}(\tilde{\mathbf{s}}_{hr}) + \iota_{B_1^{0,\eta_l}}(\tilde{\mathbf{s}}_{lr}) + \iota_{B_1^{0,\eta_l}}(\tilde{\mathbf{s}}_{lt}), \end{aligned} \quad (12)$$

$$\text{s.t.} \quad \begin{cases} \mathbf{z}_1 = \mathbf{W}\mathbf{D}\tilde{\mathbf{h}}_r, \\ \mathbf{z}_2 = \mathbf{W}\mathbf{D}\tilde{\mathbf{h}}_t, \\ \mathbf{z}_3 = \mathbf{W}\mathbf{D}\tilde{\mathbf{h}}_r - \mathbf{W}\mathbf{D}\tilde{\mathbf{h}}_t, \\ \mathbf{z}_4 = \tilde{\mathbf{h}}_r + \tilde{\mathbf{s}}_{hr}, \\ \mathbf{z}_5 = \mathbf{S}\mathbf{B}\tilde{\mathbf{h}}_r + \tilde{\mathbf{s}}_{lr}, \\ \mathbf{z}_6 = \mathbf{S}\mathbf{B}\tilde{\mathbf{h}}_t + \tilde{\mathbf{s}}_{lt}. \end{cases}$$

Then, by defining

$$\begin{aligned} g_1(\tilde{\mathbf{h}}_r) &= 0, \quad g_2(\tilde{\mathbf{h}}_t) = \sum_{b=1}^B \iota_{S^{N_h \mathbf{1}^\top [\tilde{\mathbf{l}}_t]_b / N_l}}([\tilde{\mathbf{h}}_t]_b), \\ g_3(\tilde{\mathbf{s}}_{hr}) &= \iota_{B_1^{0,\eta_h}}(\tilde{\mathbf{s}}_{hr}), \quad g_4(\tilde{\mathbf{s}}_{lr}) = \iota_{B_1^{0,\eta_l}}(\tilde{\mathbf{s}}_{lr}), \\ g_5(\tilde{\mathbf{s}}_{lt}) &= \iota_{B_1^{0,\eta_l}}(\tilde{\mathbf{s}}_{lt}), \quad h_1(\mathbf{z}_1) = \|\mathbf{z}_1\|_{1,2}, \\ h_2(\mathbf{z}_2) &= \lambda \|\mathbf{z}_2\|_{1,2}, \quad h_3(\mathbf{z}_3) = \iota_{B_q^{0,\alpha}}(\mathbf{z}_3), \\ h_4(\mathbf{z}_4) &= \iota_{B_2^{\mathbf{h}_r, \varepsilon_h}}(\mathbf{z}_4), \quad h_5(\mathbf{z}_5) = \iota_{B_2^{\mathbf{l}_r, \varepsilon_l}}(\mathbf{z}_5), \\ h_6(\mathbf{z}_6) &= \iota_{B_2^{\mathbf{l}_t, \varepsilon_l}}(\mathbf{z}_6), \end{aligned}$$

we reduce (12) to (2).

The algorithm for solving (10) is summarized in Algorithm 1. The stepsizes are determined based on OVDP [42] as follows:

$$\begin{aligned}\gamma_{1,1} &= \frac{1}{2\|\mathbf{W}\mathbf{D}\|_{\text{op}}^2 + \|\mathbf{I}\|_{\text{op}}^2 + \|\mathbf{S}\mathbf{B}\|_{\text{op}}^2} = \frac{1}{32w_{\text{max}}^2 + 2}, \\ \gamma_{1,2} &= \frac{1}{2\|\mathbf{W}\mathbf{D}\|_{\text{op}}^2 + \|\mathbf{S}\mathbf{B}\|_{\text{op}}^2} = \frac{1}{32w_{\text{max}}^2 + 1}, \\ \gamma_{1,3} &= \gamma_{1,4} = \gamma_{1,5} = \frac{1}{\|\mathbf{I}\|_{\text{op}}^2} = 1, \\ \gamma_{2,i} &= \frac{1}{5}, \text{ for } i = 1, \dots, 6,\end{aligned}\quad (13)$$

where $w_{\text{max}} := \max_{i,j,p} w_{i,j}^{(p)}$.

We should note that the algorithm does not strictly solve the original optimization problem in (10). Although the first constraint in (10), i.e., TGEC, includes a parameter α treated as a fixed constant, the algorithm instead updates α at each iteration (line 19) as follows:

$$\alpha^{(n)} \leftarrow c_\alpha \|\mathbf{W}\mathbf{D}\tilde{\mathbf{h}}_r^{(n+1)}\|_q \cdot \|\mathbf{l}_r - \mathbf{l}_t\|_1 / N_l, \quad (14)$$

where c_α is a hyperparameter. TGEC is designed to promote similarity in edge locations across time. However, the appropriate value of the threshold α in TGEC depends not only on edge alignment but also on the following two factors:

- the degree of temporal changes in spectral brightness,
- the edge strength and density of the target area.

While the first factor can be estimated from the input LR images via $\|\mathbf{l}_r - \mathbf{l}_t\|_1 / N_l$, the second factor cannot be reliably measured from the observed HR image \mathbf{h}_r due to strong noise contamination. To address this, we exploit the progressively denoised intermediate estimate $\tilde{\mathbf{h}}_r^{(n+1)}$ to compute $\|\mathbf{W}\mathbf{D}\tilde{\mathbf{h}}_r^{(n+1)}\|_q$, which is considered to reflect the edge strength and density of the target area as the noise is reduced. As a result, $\alpha^{(n)}$ is refined adaptively during the optimization, allowing the constraint strictness to be adjusted appropriately over iterations.

From a theoretical perspective, if α is fixed at any intermediate iteration, the algorithm can be regarded as solving a convex optimization problem with a fixed constraint, and it is guaranteed to converge to its optimal solution. Experimentally, we observe that the variation in $\alpha^{(n)}$ becomes negligible as the iterations proceed, and the algorithm exhibits convergent behavior (see detail in Sec. IV-F). Therefore, in practical applications, the algorithm can be used reliably without the need to explicitly fix α during the optimization process. The selection of the hyperparameter c_α will be discussed in detail in Sec. IV-E4.

IV. EXPERIMENTS

We demonstrate the effectiveness of our ST fusion method, TSSTF, through comprehensive experiments using simulated and real data for five sites. Our experiments aim to verify the following three items.

- TSSTF is as effective as state-of-the-art ST fusion methods in noiseless cases and outperforms them in noisy

Algorithm 1 P-PDS-based solver for (10)

Require: $\lambda, c_\alpha, \beta_b, \varepsilon_h, \varepsilon_l, \eta_h, \eta_l$
Ensure: $\tilde{\mathbf{h}}_r^{(n)}, \tilde{\mathbf{h}}_t^{(n)}, \tilde{\mathbf{s}}_{hr}^{(n)}, \tilde{\mathbf{s}}_{lr}^{(n)}, \tilde{\mathbf{s}}_{lt}^{(n)}$

- 1: Initialize $\tilde{\mathbf{h}}_r^{(0)}, \tilde{\mathbf{h}}_t^{(0)}, \tilde{\mathbf{s}}_{hr}^{(0)}, \tilde{\mathbf{s}}_{lr}^{(0)}, \tilde{\mathbf{s}}_{lt}^{(0)}, \mathbf{z}_j^{(0)} (j = 1, \dots, 6)$;
- 2: Set $\gamma_{1,i} (i = 1, \dots, 3), \gamma_{2,j} (j = 1, \dots, 6)$, as in (13);
- 3: **while** until a stopping criterion is not satisfied **do**
- 4: $\mathbf{u}_r \leftarrow \mathbf{D}^\top \mathbf{W}^\top \mathbf{z}_1^{(n)} + \mathbf{D}^\top \mathbf{W}^\top \mathbf{z}_3^{(n)} + \mathbf{z}_4^{(n)} + \mathbf{B}^\top \mathbf{S}^\top \mathbf{z}_5^{(n)}$
- 5: $\mathbf{u}_t \leftarrow \mathbf{D}^\top \mathbf{W}^\top \mathbf{z}_2^{(n)} - \mathbf{D}^\top \mathbf{W}^\top \mathbf{z}_3^{(n)} + \mathbf{B}^\top \mathbf{S}^\top \mathbf{z}_6^{(n)}$
- 6: $\tilde{\mathbf{h}}_r^{(n+1)} \leftarrow \tilde{\mathbf{h}}_r^{(n)} - \gamma_{1,1} \mathbf{u}_r$
- 7: $\tilde{\mathbf{h}}_t^{(n+1)} \leftarrow \tilde{\mathbf{h}}_t^{(n)} - \gamma_{1,2} \mathbf{u}_t$
- 8: **for** $b = 1, \dots, B$ **do**
- 9: $[\tilde{\mathbf{h}}_t^{(n+1)}]_b \leftarrow P_{S_{N_h, \beta_b}^{\top} [\tilde{\mathbf{h}}_t]_b / N_l}([\tilde{\mathbf{h}}_t^{(n+1)}]_b)$
- 10: **end for**
- 11: $\tilde{\mathbf{s}}_{hr}^{(n+1)} \leftarrow P_{B_1^{0, \eta_h}}(\tilde{\mathbf{s}}_{hr}^{(n)} - \gamma_{1,3} \mathbf{z}_4)$
- 12: $\tilde{\mathbf{s}}_{lr}^{(n+1)} \leftarrow P_{B_1^{0, \eta_l}}(\tilde{\mathbf{s}}_{lr}^{(n)} - \gamma_{1,4} \mathbf{z}_5)$
- 13: $\tilde{\mathbf{s}}_{lt}^{(n+1)} \leftarrow P_{B_1^{0, \eta_l}}(\tilde{\mathbf{s}}_{lt}^{(n)} - \gamma_{1,5} \mathbf{z}_6)$
- 14: $\mathbf{v}_r \leftarrow 2\tilde{\mathbf{h}}_r^{(n+1)} - \tilde{\mathbf{h}}_r^{(n)}$
- 15: $\mathbf{v}_t \leftarrow 2\tilde{\mathbf{h}}_t^{(n+1)} - \tilde{\mathbf{h}}_t^{(n)}$
- 16: $\mathbf{w}_{hr} \leftarrow 2\tilde{\mathbf{s}}_{hr}^{(n+1)} - \tilde{\mathbf{s}}_{hr}^{(n)}$
- 17: $\mathbf{w}_{lr} \leftarrow 2\tilde{\mathbf{s}}_{lr}^{(n+1)} - \tilde{\mathbf{s}}_{lr}^{(n)}$
- 18: $\mathbf{w}_{lt} \leftarrow 2\tilde{\mathbf{s}}_{lt}^{(n+1)} - \tilde{\mathbf{s}}_{lt}^{(n)}$
- 19: $\alpha^{(n)} \leftarrow c_\alpha \|\mathbf{W}\mathbf{D}\tilde{\mathbf{h}}_r^{(n+1)}\|_q \cdot \|\mathbf{l}_r - \mathbf{l}_t\|_1 / N_l$
- 20: $\mathbf{z}_1^{(n)} \leftarrow \mathbf{z}_1^{(n)} + \gamma_{2,1} \mathbf{W}\mathbf{D}\mathbf{v}_r$
- 21: $\mathbf{z}_2^{(n)} \leftarrow \mathbf{z}_2^{(n)} + \gamma_{2,2} \mathbf{W}\mathbf{D}\mathbf{v}_t$
- 22: $\mathbf{z}_3^{(n)} \leftarrow \mathbf{z}_3^{(n)} + \gamma_{2,3} (\mathbf{W}\mathbf{D}\mathbf{v}_r - \mathbf{W}\mathbf{D}\mathbf{v}_t)$
- 23: $\mathbf{z}_4^{(n)} \leftarrow \mathbf{z}_4^{(n)} + \gamma_{2,4} (\mathbf{v}_r + \mathbf{w}_{hr})$
- 24: $\mathbf{z}_5^{(n)} \leftarrow \mathbf{z}_5^{(n)} + \gamma_{2,5} (\mathbf{S}\mathbf{B}\mathbf{v}_r + \mathbf{w}_{lr})$
- 25: $\mathbf{z}_6^{(n)} \leftarrow \mathbf{z}_6^{(n)} + \gamma_{2,6} (\mathbf{S}\mathbf{B}\mathbf{v}_t + \mathbf{w}_{lt})$
- 26: $\mathbf{z}_1^{(n+1)} \leftarrow \mathbf{z}_1^{(n)} - \gamma_{2,1} \text{prox}_{\frac{1}{\gamma_{2,1}} \|\cdot\|_{1,2}}(\frac{1}{\gamma_{2,1}} \mathbf{z}_1^{(n)})$
- 27: $\mathbf{z}_2^{(n+1)} \leftarrow \mathbf{z}_2^{(n)} - \gamma_{2,2} \text{prox}_{\frac{\lambda}{\gamma_{2,2}} \|\cdot\|_{1,2}}(\frac{1}{\gamma_{2,2}} \mathbf{z}_2^{(n)})$
- 28: $\mathbf{z}_3^{(n+1)} \leftarrow \mathbf{z}_3^{(n)} - \gamma_{2,3} P_{B_q^{0, \alpha^{(n)}}}(\frac{1}{\gamma_{2,3}} \mathbf{z}_3^{(n)})$
- 29: $\mathbf{z}_4^{(n+1)} \leftarrow \mathbf{z}_4^{(n)} - \gamma_{2,4} P_{B_2^{h_r, \varepsilon_h}}(\frac{1}{\gamma_{2,4}} \mathbf{z}_4^{(n)})$
- 30: $\mathbf{z}_5^{(n+1)} \leftarrow \mathbf{z}_5^{(n)} - \gamma_{2,5} P_{B_2^{l_r, \varepsilon_l}}(\frac{1}{\gamma_{2,5}} \mathbf{z}_5^{(n)})$
- 31: $\mathbf{z}_6^{(n+1)} \leftarrow \mathbf{z}_6^{(n)} - \gamma_{2,6} P_{B_2^{l_t, \varepsilon_l}}(\frac{1}{\gamma_{2,6}} \mathbf{z}_6^{(n)})$
- 32: $n \leftarrow n + 1$
- 33: **end while**

cases. We conducted comparative experiments on four cases of noise contamination. The experimental results for simulated data and real data are presented in Sec. IV-C and Sec. IV-D, respectively.

- The parameters of TSSTF can be set independently of target regions or noise levels. As detailed in Sec. IV-E, we extensively varied each parameter and found a recommended value that yields consistently high performance.
- The algorithm converges stably. We analyze the behavior of the TSSTF algorithm in Sec. IV-F, demonstrating that the adaptive update of $\alpha^{(n)}$ stabilizes during optimization and that the algorithm converges without explicitly fixing α at an intermediate iteration.

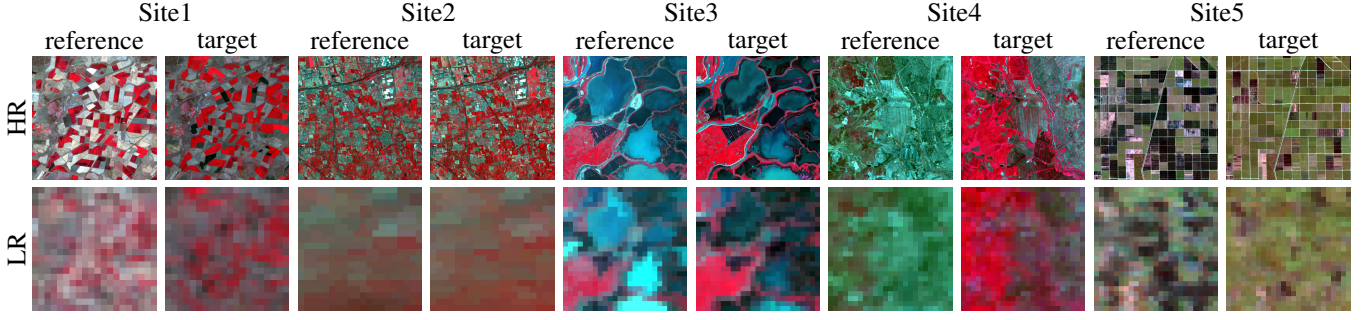


Fig. 6. Visualization of the real HR and LR satellite images used for five experimental sites (Site1–Site5). For each site, reference and target images are shown side-by-side. The HR images are taken from Landsat, while the LR images are from MODIS.

TABLE I
THE PARAMETER SETTING

Parameter	Equation	Value / Setting
δ	(6)	0.1
k	(6)	2
c_α	(14)	5
q	(9)	the mixed $\ell_{1,2}$ -norm
λ	(10)	1
β_b	(10)	$\left \frac{1}{N_l} \mathbf{1}^\top [\mathbf{l}_r]_b - \frac{1}{N_h} \mathbf{1}^\top [\mathbf{h}_r]_b \right $
ε_h	(10)	$0.98\sigma_h \sqrt{N_h B(1 - r_h)}$
ε_l	(10)	$\ \mathbf{l}_r - \mathbf{S}\mathbf{B}\mathbf{h}_r\ _2$
η_h	(10)	$0.49N_h r_h$
η_l	(10)	$0.49N_l r_l$

TABLE II
NOISE SETTING

Cases	Gaussian	Salt-and-pepper
Case 1	–	–
Case 2	$\sigma_h = 0.05$	–
Case 3	$\sigma_h = 0.05$	$r_h = 0.02$
Case 4	$\sigma_h = 0.05$	$r_h = 0.05$

A. Data Description

We evaluated our method using real MODIS and Landsat time-series images from five different geographical sites, which we denote as Site1 to Site5. The corresponding high-resolution (HR) and low-resolution (LR) images at each site are shown in Fig. 6. The data for Site1, Site2, and Sites3–5 were obtained from [52], [53], and [54], respectively. The native spatial resolutions of Landsat and MODIS images are 30-m and 500-m, respectively, and are not integer multiples of each other. Since most ST fusion methods assume an integer resolution ratio between HR and LR images, data providers commonly resample MODIS images so their spatial resolution is an integer multiple of Landsat's. In the datasets used in this study, the resolution ratio between the Landsat (HR) and resampled MODIS (LR) images is adjusted to 20:1 for Site1 and Site2, and to 16:1 for Site3, Site4, and Site5.

We also conducted experiments on simulated data. In the case of real satellite observations, radiometric and geometric inconsistencies exist between different sensors. This means

TABLE III
EXISTING METHODS

Approach		Number of reference dates	Robustness to noise	
			Gaussian	Sparse
STARFM [9]	Rule	1	–	–
VIPSTF [17]	Rule	1	–	–
RSFN [24]	Learning	2	✓	–
RobOt [29]	Optimization	1	–	–
SwinSTFM [27]	Learning	1	–	–
ROSTF [30]	Optimization	1	✓	✓
TSSTF	Optimization	1	✓	✓

that the pure fusion capability of each method cannot be accurately evaluated in experiments using real data because these inconsistencies affect performance, as also addressed in [16]. Therefore, we additionally conducted experiments on simulated data generated based on our observation model. Specifically, the simulated LR images were generated from the corresponding real HR images using the model in (4) with no modelling error ($\mathbf{m} = \mathbf{0}$), while the real HR images were used as HR images.

To verify the noise robustness, we tested four cases with different noise settings on the observed HR images, as summarized in Table II. Specifically, Gaussian noise with standard deviation σ_h and salt-and-pepper noise with a superimposition ratio r_h were added to the HR images. The LR images were kept noise-free in all cases.

B. Experimental Setup

The parameters in our method were set as shown in Table I. Among them, δ , k , c_α , and q were heuristically determined by empirical tuning to achieve favorable fusion performance consistently across various sites and noise conditions. The details of these parameter searches are provided in Sec. IV-E. The maximum number of iterations for Algorithm 1 was fixed at 10000. The stopping criterion of Algorithm 1 was defined as $\|\tilde{\mathbf{h}}_r^{(n)} - \tilde{\mathbf{h}}_r^{(n-1)}\|_2 / \|\tilde{\mathbf{h}}_r^{(n-1)}\|_2 < 10^{-5}$, $\|\tilde{\mathbf{h}}_t^{(n)} - \tilde{\mathbf{h}}_t^{(n-1)}\|_2 / \|\tilde{\mathbf{h}}_t^{(n-1)}\|_2 < 10^{-5}$, $\|\mathbf{l}_r - \mathbf{S}\mathbf{B}\tilde{\mathbf{h}}_r^{(n)}\|_2 \leq \varepsilon_l$, and $\|\mathbf{l}_t - \mathbf{S}\mathbf{B}\tilde{\mathbf{h}}_t^{(n)}\|_2 \leq \varepsilon_l$.

The spatial spread transform matrix \mathbf{B} in (4) was implemented as a blurring operator with an averaging filter of size s . The downsampling matrix \mathbf{S} in (4) was designed to extract the center pixel value in the $s \times s$ window. The window size s was set to 20 for the Site1 and Site2 data, while it was set to

TABLE IV
THE PSNR AND MSSIM RESULTS IN THE EXPERIMENTS WITH SIMULATED DATA

Site	Noise	Metrics	STARFM [9]	VIPSTF [17]	RSFN [24]	RobOt [29]	SwinSTFM [27]	ROSTF [30]	TSSTF (Ours)
Site1	Case1	PSNR	26.1975	27.1537	22.5310	<u>27.4072</u>	25.6272	25.0878	29.7199
		MSSIM	0.7525	<u>0.7923</u>	0.6329	0.7773	0.7458	0.7267	0.8198
	Case2	PSNR	22.4483	24.8582	22.4539	23.8878	24.9553	<u>26.0617</u>	29.4261
		MSSIM	0.3862	0.5450	0.6259	0.4433	0.6417	<u>0.7334</u>	0.7926
	Case3	PSNR	19.1372	22.3166	22.4578	20.6883	24.2255	<u>26.4067</u>	29.1464
		MSSIM	0.2756	0.4223	0.6187	0.3296	0.5426	<u>0.7379</u>	0.7856
	Case4	PSNR	16.6554	20.2517	22.3949	18.2197	23.3377	<u>26.5683</u>	28.6891
		MSSIM	0.1777	0.3038	0.6068	0.2198	0.4512	<u>0.7394</u>	0.7744
Site2	Case1	PSNR	33.6744	33.3978	25.0700	33.5095	30.7136	33.3471	33.5747
		MSSIM	0.9015	0.8996	0.5312	<u>0.9003</u>	0.8203	0.8926	0.8968
	Case2	PSNR	25.1557	24.9029	22.3207	25.3139	28.2861	<u>30.1577</u>	30.3996
		MSSIM	0.4841	0.4727	0.3777	0.4937	0.6812	<u>0.7281</u>	0.7373
	Case3	PSNR	19.7309	19.4758	22.2670	19.7843	26.6921	<u>29.5592</u>	29.8369
		MSSIM	0.3438	0.3358	0.3712	0.3486	0.5766	<u>0.6997</u>	0.7174
	Case4	PSNR	16.6600	16.4069	22.1988	16.7170	25.1585	<u>28.0978</u>	29.2198
		MSSIM	0.2215	0.2166	0.3714	0.2244	0.4794	<u>0.6537</u>	0.6925
Site3	Case1	PSNR	<u>26.7925</u>	26.8487	21.4700	26.4423	24.5716	26.0320	26.5860
		MSSIM	0.7472	0.7639	0.5024	<u>0.7626</u>	0.6585	0.7521	0.7553
	Case2	PSNR	22.5151	24.6884	21.5191	23.0681	24.0418	<u>25.9846</u>	26.4425
		MSSIM	0.3238	0.4726	0.4901	0.3870	0.5476	0.7277	0.7264
	Case3	PSNR	18.5422	21.5184	21.4037	19.4127	23.5476	<u>26.0269</u>	26.5958
		MSSIM	0.2350	0.3532	0.4783	0.2881	0.4731	<u>0.7246</u>	0.7260
	Case4	PSNR	15.8839	19.0860	21.4498	16.8165	22.9400	<u>26.0031</u>	26.5036
		MSSIM	0.1564	0.2411	0.4829	0.1884	0.4037	<u>0.7215</u>	0.7222
Site4	Case1	PSNR	29.6249	<u>29.6803</u>	23.5304	28.1509	27.8372	29.1143	30.3920
		MSSIM	0.7271	<u>0.7518</u>	0.6303	0.6995	0.7123	0.7149	0.7552
	Case2	PSNR	23.4362	24.9770	22.2002	23.2133	26.7451	<u>29.7295</u>	30.1514
		MSSIM	0.2964	0.3881	0.5685	0.3167	0.5914	<u>0.7240</u>	0.7298
	Case3	PSNR	19.1252	20.7111	24.0856	19.2004	25.8221	<u>29.8360</u>	30.1435
		MSSIM	0.2036	0.2747	0.5653	0.2224	0.5061	<u>0.7250</u>	0.7296
	Case4	PSNR	16.4238	17.9716	21.8361	16.6427	24.6637	<u>29.7602</u>	29.9186
		MSSIM	0.1242	0.1745	0.5582	0.1386	0.4222	<u>0.7216</u>	0.7255
Site5	Case1	PSNR	26.2623	<u>26.4037</u>	20.2229	24.4367	23.0449	24.7979	26.6491
		MSSIM	0.6990	<u>0.6722</u>	0.5459	0.6657	0.6479	<u>0.7042</u>	0.7322
	Case2	PSNR	22.1295	<u>26.0215</u>	19.6438	20.8910	22.5311	24.9989	26.2188
		MSSIM	0.3164	<u>0.6301</u>	0.4891	0.2862	0.5228	<u>0.6964</u>	0.7026
	Case3	PSNR	18.4586	<u>25.5353</u>	20.7984	17.7675	22.2331	25.0057	26.2674
		MSSIM	0.2227	<u>0.5829</u>	0.5125	0.2054	0.4347	<u>0.6891</u>	0.7007
	Case4	PSNR	15.9753	24.9664	19.4596	15.6715	21.7079	<u>24.9890</u>	26.0682
		MSSIM	0.1409	0.5274	0.4721	0.1374	0.3558	<u>0.6871</u>	0.6949

16 for the Site3, Site4, and Site5 data, reflecting the difference in spatial resolution between the Landsat and MODIS images.

For the quantitative evaluation, we used the following two metrics: the peak-to-noise ratio (PSNR):

$$\text{PSNR} = 10 \log_{10} \left(\frac{1}{\sqrt{\frac{1}{N_h B} \|\tilde{\mathbf{h}}_t - \hat{\mathbf{h}}_t\|_2^2}} \right),$$

where $\tilde{\mathbf{h}}_t$ and $\hat{\mathbf{h}}_t$ denote an estimated HR image and a ground-truth HR image, respectively, on the target date; the mean

structural similarity overall bands (MSSIM) [55]:

$$\text{MSSIM} = \frac{1}{B} \sum_{b=1}^B \text{SSIM} \left([\tilde{\mathbf{h}}_t]_b, [\hat{\mathbf{h}}_t]_b \right).$$

PSNR was calculated to measure the difference between the estimated image and the ground-truth at the pixel level. MSSIM was used to evaluate the similarity of the overall structure. Higher these values indicate better estimation performance.

Our method was compared with STARFM [9], VIPSTF [17], RSFN [24], RobOt [29], SwinSTFM [27], and ROSTF [30]. Table III summarizes the characteristics of these methods and TSSTF. Among existing methods, ROSTF is

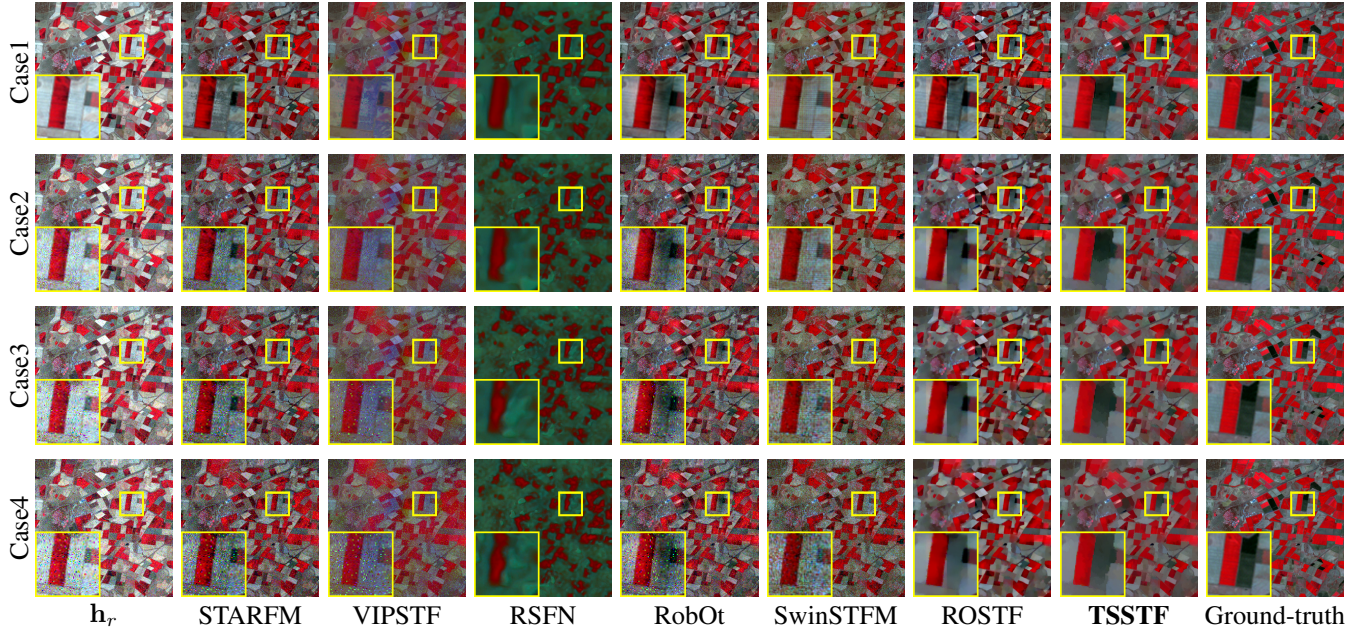


Fig. 7. ST fusion results for the Site1 simulated data. The results from top to bottom correspond to Case 1, Case 2, Case 3, and Case 4, respectively.

the only method that can deal with mixed Gaussian and sparse noise. RSFN is designed to be robust to Gaussian noise. However, it assumes the noise is localized rather than distributed across the entire image, which is unrealistic. Furthermore, RSFN requires HR-LR image pairs obtained on two reference dates before and after the target date. This requirement for future observations does not align with the fundamental goal of ST fusion, which aims to estimate the HR image at the target time using only currently available or earlier observations. To ensure a fair comparison in our experimental setting, where only a single past reference date is available, we adapted RSFN by using the same HR-LR image pair as both the preceding and following reference. For each existing method, we used the parameter values recommended in the corresponding reference.

C. Experimental Results with Simulated Data

Table IV shows the PSNR and MSSIM results in experiments with the simulated data. The best and second-best results are highlighted in bold and underlined, respectively. Under the noise-free condition (Case 1), our TSSTF achieves performance comparable to or better than existing methods across all sites. This indicates that TSSTF is already highly effective as a pure ST fusion method, even without considering its robustness to noise. When Gaussian and salt-and-pepper noise is added (Cases 2–4), the performance of STARFM, VIPSTF, RobOt, and SwinSTFM drops significantly, as these methods do not account for noise. In contrast, the noise-robust methods, including ROSTF and TSSTF, maintain stable performance even under noisy conditions. Notably, TSSTF achieves the highest PSNR in all noise-contaminated cases across all sites, and yields the highest MSSIM scores in all conditions except for one. This consistent superiority highlights its robustness to noise and its ability to accurately preserve spatial structure. RSFN consistently yields relatively low

performance under both noise-free and noise-contaminated conditions, due to its input requirement for a future reference, which is impractical and incompatible with that of our method.

Fig. 7 shows the estimated results for the Site1 simulated data. We first focus on the results in the noiseless case. As observed in the zoomed-in region enclosed by the yellow box, there is a significant spectral change between the reference HR image h_r and the Ground-truth. RSFN produces overly blurred results with unnatural color tones. VIPSTF suffers from severe spectral distortion. STARFM and SwinSTFM fail to capture the spectral change in the zoomed-in region, resulting in brightness that is biased toward h_r rather than the Ground-truth. While RobOt and ROSTF offer relatively better estimates, they still exhibit noticeable blurring or artifacts in fine details. In contrast, the proposed TSSTF successfully preserves both edge sharpness and spectral fidelity, yielding the most visually accurate fusion result among all methods.

We next examine the noisy cases, i.e., Case2, Case3, and Case4. STARFM, VIPSTF, RobOt, and SwinSTFM produce unstable results with noise, as they are not designed to handle noise-contaminated inputs. RSFN fails to produce reasonable outputs not only because its input requirement is incompatible with ours, but also because it is designed to address only localized Gaussian noise rather than mixed noise across the entire image. ROSTF provides more robust estimates with only a minor loss of accuracy compared to the noiseless case. However, it still suffers from oversmoothing and artifacts, as observed in the zoomed-in region. In contrast, the proposed TSSTF consistently yields the most accurate visual results across all noisy cases. These results can be attributed to our two key mechanisms: TGTv, which effectively suppresses noise while preserving spatial structure, and TGEC, which enforces the consistency of edge locations. Together, they contribute to the high spatial fidelity and robustness to noise.

TABLE V
THE PSNR AND MSSIM RESULTS IN THE EXPERIMENTS WITH REAL DATA

Site	Noise	Metrics	STARFM [9]	VIPSTF [17]	RSFN [24]	RobOt [29]	SwinSTFM [27]	ROSTF [30]	TSSTF (Ours)
Site1	Case1	PSNR	24.3788	26.3178	22.1053	25.2970	<u>25.4539</u>	24.0446	25.4071
		MSSIM	0.7188	<u>0.7705</u>	0.6331	0.7617	0.7477	0.7264	0.7834
	Case2	PSNR	21.6239	24.5892	21.7240	22.7659	<u>24.7426</u>	24.4584	25.5327
		MSSIM	0.3717	0.5598	0.6149	0.4354	0.6400	<u>0.7255</u>	0.7508
	Case3	PSNR	18.6567	22.3522	21.6843	20.0431	24.0007	<u>24.5562</u>	25.3800
		MSSIM	0.2660	0.4452	0.6084	0.3230	0.5396	<u>0.7229</u>	0.7431
	Case4	PSNR	16.3835	20.5153	21.6955	17.8456	23.1372	<u>24.6468</u>	25.2688
		MSSIM	0.1745	0.3352	0.6002	0.2171	0.4490	<u>0.7194</u>	0.7354
Site2	Case1	PSNR	32.5489	30.4999	25.3723	32.3656	30.5518	32.4981	32.3516
		MSSIM	0.8940	0.8467	0.5617	0.8939	0.8218	0.8963	<u>0.8945</u>
	Case2	PSNR	25.0082	26.4936	21.9431	25.1019	28.0853	<u>29.2635</u>	29.7290
		MSSIM	0.4810	0.5577	0.3622	0.4901	0.6804	<u>0.7175</u>	0.7329
	Case3	PSNR	19.7472	22.2439	21.8374	19.7672	26.5864	<u>28.7685</u>	29.5344
		MSSIM	0.3439	0.4173	0.3515	0.3485	0.5781	<u>0.6880</u>	0.7152
	Case4	PSNR	16.5838	19.3812	21.8948	16.6188	25.1137	<u>28.8078</u>	29.0788
		MSSIM	0.2170	0.2801	0.3592	0.2196	0.4772	<u>0.6739</u>	0.6898
Site3	Case1	PSNR	24.6057	<u>25.7173</u>	21.4036	24.7815	24.6716	25.6246	26.2478
		MSSIM	0.6876	<u>0.7191</u>	0.5014	0.7162	0.6655	<u>0.7347</u>	0.7362
	Case2	PSNR	21.7784	24.6417	21.3639	22.4301	24.1281	25.5741	26.0362
		MSSIM	0.3124	0.5417	0.4819	0.3924	0.5585	0.7078	<u>0.7062</u>
	Case3	PSNR	18.2775	22.5823	21.5174	19.3547	23.5658	25.6242	26.0761
		MSSIM	0.2290	0.4385	0.4838	0.2999	0.4854	0.7050	<u>0.7039</u>
	Case4	PSNR	15.7116	20.6533	21.3433	16.9134	22.8930	25.5968	26.0389
		MSSIM	0.1510	0.3280	0.4752	0.1945	0.4113	<u>0.7005</u>	0.7012
Site4	Case1	PSNR	<u>27.8198</u>	28.1865	23.3897	26.5057	26.9938	26.9786	27.4466
		MSSIM	0.7042	0.7375	0.6261	0.6810	0.7101	0.6757	<u>0.7263</u>
	Case2	PSNR	22.9088	24.6685	22.0970	22.6090	26.0265	<u>27.2705</u>	27.4023
		MSSIM	0.2898	0.4118	0.5673	0.3180	0.5870	<u>0.6809</u>	0.7006
	Case3	PSNR	18.9509	21.0291	23.6751	18.9970	25.3502	<u>27.3055</u>	27.3723
		MSSIM	0.2003	0.3017	0.5766	0.2266	0.5064	<u>0.6809</u>	0.6998
	Case4	PSNR	16.2974	18.5226	21.8709	16.5125	24.3862	27.1247	27.1153
		MSSIM	0.1219	0.1984	0.5549	0.1394	0.4254	<u>0.6728</u>	0.6963
Site5	Case1	PSNR	25.5783	<u>25.8931</u>	20.2998	24.0170	22.8935	24.5551	25.9363
		MSSIM	0.6978	<u>0.6688</u>	0.5482	0.6603	0.6470	<u>0.7025</u>	0.7291
	Case2	PSNR	21.7946	25.6877	19.5695	20.6170	22.4251	24.7140	<u>25.5289</u>
		MSSIM	0.3155	0.6364	0.4890	0.2794	0.5228	<u>0.6900</u>	0.6982
	Case3	PSNR	18.2406	<u>25.5194</u>	20.9021	17.5512	22.0790	24.7815	25.5486
		MSSIM	0.2223	<u>0.6121</u>	0.5262	0.2005	0.4300	<u>0.6890</u>	0.6949
	Case4	PSNR	15.8175	<u>25.3051</u>	19.8435	15.4844	21.5458	24.7640	25.4348
		MSSIM	0.1400	0.5836	0.4952	0.1348	0.3517	<u>0.6868</u>	0.6910

D. Experimental Results with Real Data

Table V shows the PSNR and MSSIM results in experiments with the real data. Compared to the results on the simulated data, the performance of all methods degrades due to radiometric and geometric inconsistencies between the Landsat and MODIS sensors. In the noise-free case (Case1), TSSTF achieves either the highest or second-highest score in PSNR or MSSIM across all sites. In the noisy cases (Case2–Case4), TSSTF consistently yields the best performance in PSNR or MSSIM for all sites. These results confirm that TSSTF is both effective and robust under real-world conditions.

Fig. 8 shows the estimated results for the Site5 real data. In Case1, VIPSTF produces overly blurred results. RSFN and

SwinSTFM fail to predict spectral brightness, resulting in unrealistic color representations. RobOt and ROSTF generate relatively reasonable estimates; however, they struggle to accurately capture the spectral changes from the reference image \mathbf{h}_r to the Ground-truth, especially in the region enclosed by the yellow box. STARFM and the proposed TSSTF achieve faithful reconstruction in terms of spatial structure and spectral consistency, closely matching the ground-truth image.

Under the noisy conditions, VIPSTF and RSFN exhibit further performance degradation, producing overly blurred results and/or significant spectral distortions. STARFM, RobOt, and SwinSTFM reflect the noise contained in the input images, resulting in noisy outputs. ROSTF suppresses noise to some

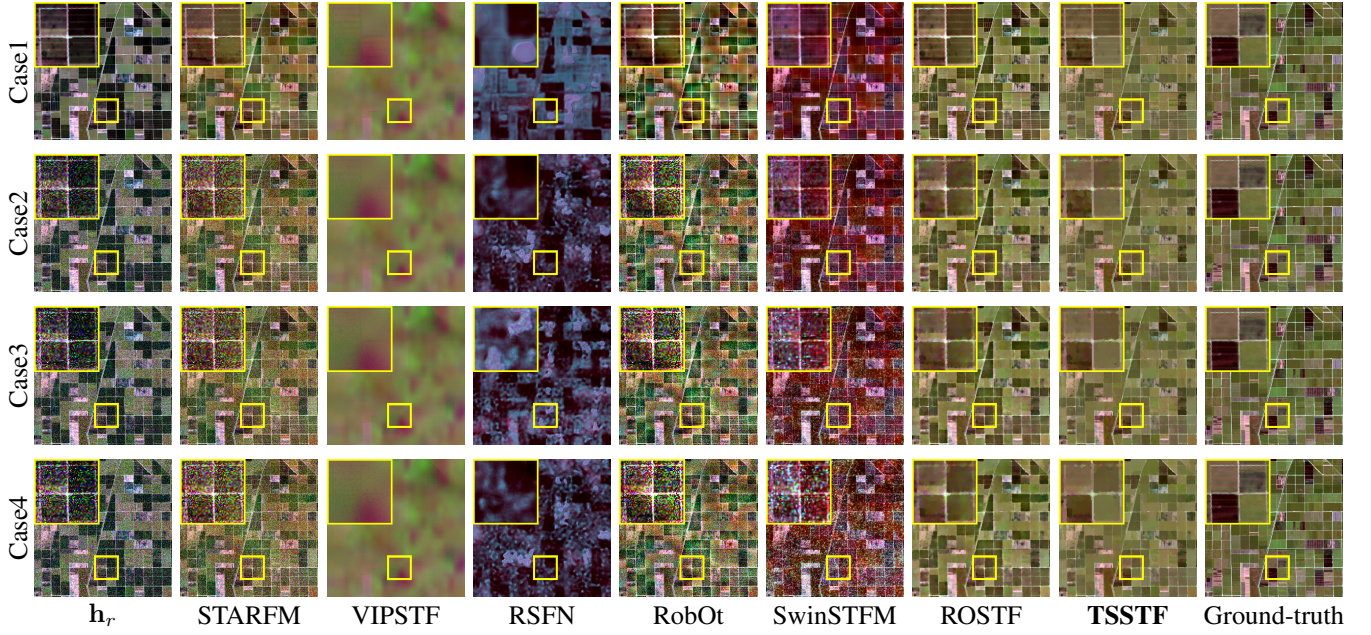


Fig. 8. ST fusion results for the Site5 real data. The results from top to bottom correspond to Case 1, Case 2, Case 3, and Case 4, respectively.

extent but it can generate unnatural artifacts. Specifically, it suffers from spectral distortion around edges, as its spatially uniform total variation regularization fails to distinguish between noise and intrinsic spatial structure. The proposed TSSTF consistently produces the most accurate results across all cases, effectively mitigating the influence of noise while faithfully reconstructing both spatial structure and spectral characteristics.

E. Facilitation of Parameter Selection

We have four parameters (δ, k, q, c_α), which were heuristically determined by empirical tuning. In this section, we present the details of comprehensive parameter searches conducted using all the data introduced in Sec. IV-A, including both simulated and real data across all five sites under all four noise cases. We provide a single recommended value for each parameter, which is robust against diverse data characteristics, such as land cover types, temporal changes in spectral brightness, and noise levels. During the search for each parameter, the other parameters were fixed to the values listed in Table I.

1) *Parameter δ in weights*: The parameter δ , defined in (6), controls the distribution of the weights. A larger δ leads to less variation among the weights, whereas a smaller δ results in greater variation. To identify an appropriate value for δ , we conducted experiments using discrete values spanning from 10^{-3} to 10^2 (i.e., $10^{-3}, 10^{-2}, 10^{-1}, 10^0, 10^1$, and 10^2). The impact of δ on performance was evaluated by averaging PSNR across all sites for each noise case (as shown in Fig. 9 (a)) and across all noise cases for each site (as depicted in Fig. 9 (b)). As observed in both figures, the performance consistently peaks at $\delta = 10^{-1}$ and then either remains stable or slightly decreases. Importantly, this trend holds across different sites and noise levels. Therefore, we recommend to set $\delta = 10^{-1}$ as the default value.

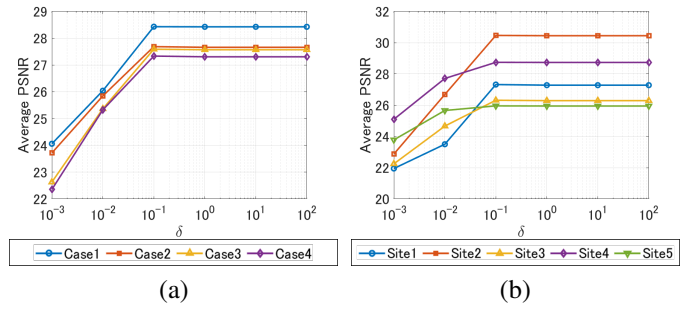


Fig. 9. Comparison of the average PSNR according to δ under different conditions. The performance of TSSTF for each noise case (a) and for each site (b).

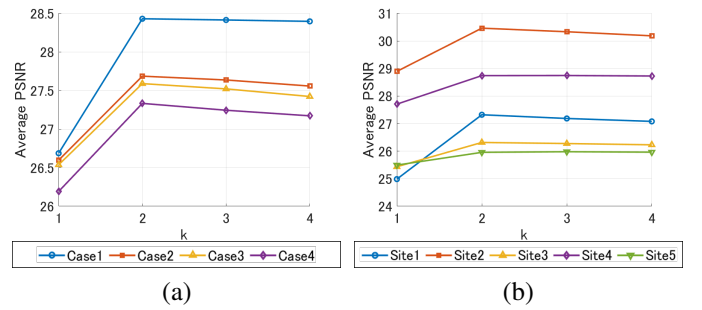


Fig. 10. Comparison of the average PSNR according to k under different conditions. The performance of TSSTF for each noise case (a) and over all noise cases for each site (b).

2) *Parameter k in weights*: The parameter k specifies how many of the four directional weights $\{w_{i,j}^{(p)}\}_{p=1}^4$ are forced to zero at each pixel (i, j) . To determine an appropriate value, we evaluated $k \in \{1, 2, 3, 4\}$ and examined the resulting PSNR averaged over all sites for each noise case (Fig. 10 (a)) and over all noise cases for each site (Fig. 10 (b)). Across all noise conditions and sites, the PSNR consistently peaks

TABLE VI
AVERAGE PSNR RESULTS WITH THE ℓ_1 , ℓ_2 , AND MIXED $\ell_{1,2}$ -NORM IN TGED ACROSS DIFFERENT NOISE CASES

	ℓ_1	ℓ_2	$\ell_{1,2}$
Case1	27.76	28.34	28.43
Case2	27.26	27.51	27.69
Case3	27.16	27.37	27.59
Case4	26.91	27.12	27.33

TABLE VII
AVERAGE PSNR RESULTS WITH THE ℓ_1 , ℓ_2 , AND MIXED $\ell_{1,2}$ -NORM IN TGED ACROSS DIFFERENT SITES

	ℓ_1	ℓ_2	$\ell_{1,2}$
Site1	26.66	26.83	27.32
Site2	30.48	30.47	30.47
Site3	25.63	26.12	26.32
Site4	28.41	28.74	28.74
Site5	25.21	25.78	25.96

at $k = 2$, indicating that setting $k = 2$ provides robust performance against diverse data characteristics. These results suggest that selecting only two dominant directions per pixel is more effective for capturing intrinsic spatial structure while distinguishing it from noise, than using all four directions indiscriminately.

3) *Norm q in TGED*: We considered three options for the TGED norm q in (9), namely the ℓ_1 -norm, the ℓ_2 -norm, and the mixed $\ell_{1,2}$ -norm. Table VI shows the average PSNR results with the three types of TGED norm across different noise conditions. It is found that our TSSTF yields the highest PSNR with the mixed $\ell_{1,2}$ -norm under every noise condition. Table VII reports the average PSNR results for each site. the mixed $\ell_{1,2}$ -norm gives the best performance at Site1, Site3, Site4, and Site5, whereas no significant difference is observed at Site2. These results indicate that the mixed $\ell_{1,2}$ -norm provides robust and stable performance regardless of target area or noise levels. Based on these observations, we recommend setting the TGED norm to the mixed $\ell_{1,2}$ in practice.

4) *Coefficient c_α in TGED*: We have a parameter c_α in (14) to control the threshold α for TGED, which regulates the degree of edge location similarity. To determine an appropriate value for c_α , we evaluated the performance of TSSTF with values of c_α ranging from 0.1 to 10 (specifically, 0.1, 1, 2, 3, 4, 5, 6, 7, 8, 9, and 10). Fig. 11 (a) presents the average PSNR results across all sites for each noise case, while Fig. 11 (b) shows the average PSNR results across all noise cases for each site. These results demonstrate that TSSTF consistently achieves high performance when c_α is set around 5, regardless of input data. This robustness can be attributed to the α setting in (14), which accounts for temporal changes in spectral brightness, spatial structural complexity of input data, and is designed to adapt to different noise levels.

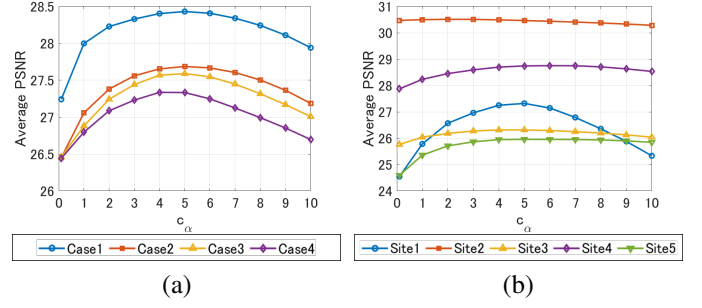


Fig. 11. Comparison of the average PSNR according to c_α under different conditions. The performance of TSSTF for each noise case (a) and for each site (b).

F. Algorithm Convergence

We investigate the dynamic behavior of the TSSTF algorithm during the optimization process. Specifically, we track three quantities at each iteration n :

- the adaptive threshold $\alpha^{(n)}$ for TGED defined in (14),
- the update error for $\tilde{\mathbf{h}}_t$, defined as $\|\tilde{\mathbf{h}}_t^{(n)} - \tilde{\mathbf{h}}_t^{(n-1)}\|_2 / \|\tilde{\mathbf{h}}_t^{(n-1)}\|_2$,
- the PSNR values, calculated between the intermediate estimate $\tilde{\mathbf{h}}_t^{(n)}$ and the ground-truth $\tilde{\mathbf{h}}_t$.

Fig. 12 shows their transitions for real data under four noise cases. Each curve corresponds to one site.

In the noise-free setting (Case1), $\alpha^{(n)}$ remains constant because the observed reference HR image \mathbf{h}_r is fully trusted and the estimate $\tilde{\mathbf{h}}_r$ therefore is not updated. Under noise contamination (Cases 2–4), $\alpha^{(n)}$ is adaptively updated by the rule in (14). After roughly 1,000 iterations, however, these adjustments cease almost entirely and $\alpha^{(n)}$ stabilizes. From that point on, the algorithm can be regarded as solving a constrained optimization problem with a fixed α , and it is expected to converge to its optimal solution.

This stable evolution of $\alpha^{(n)}$ arises because the intermediate estimate $\tilde{\mathbf{h}}_r^{(n+1)}$ is gradually denoised through iterations. After a sufficient number of iterations, the quantity $\|\mathbf{W}\mathbf{D}\tilde{\mathbf{h}}_r^{(n+1)}\|_{1,2}$ settles to a value that reflects the intrinsic edge strength and density of the target scene. Although the appropriate strictness of TGED cannot be determined in advance due to strong noise, this adaptive setting avoids the need to pre-select a fixed α , allowing the algorithm to self-tune across diverse noise conditions.

As show in the middle and bottom rows of Fig. 12, the update error decreases almost monotonically in all cases, and the PSNR curve flattens out after approximately 2,000 iterations. These results confirm that the proposed algorithm reliably converges without the need to explicitly fix α at an intermediate iteration.

V. CONCLUSION

We have proposed a novel ST fusion framework, named Temporally-Similar Structure-Aware ST Fusion (TSSTF), which achieves noise-robust ST fusion while preserving fine spatial structure in high spatial resolution satellite images. TSSTF is built upon two key components: temporally-guided

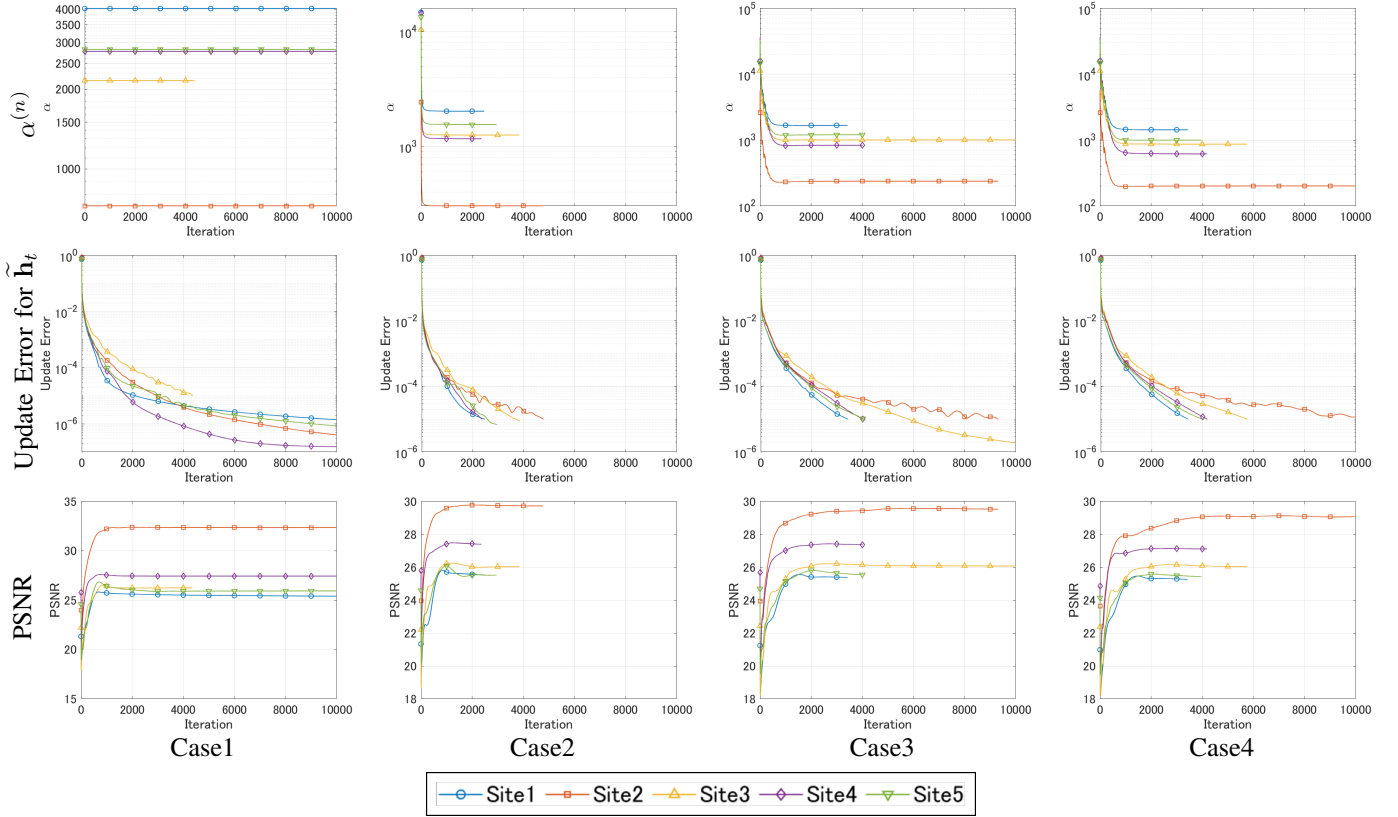


Fig. 12. Behavior of the TSSTF algorithm for real data across different noise cases. The top, middle, and bottom rows show the transitions of $\alpha^{(n)}$, the update error for \mathbf{h}_t , and the PSNR values, respectively. Each curve represents each site data.

total variation (TGTv) and temporally-guided edge constraint (TGEc). TGTv promotes spatial piecewise smoothness guided by the structural information of the reference image, while TGEc enforces consistency in edge locations across time, allowing for spectral changes. We formulated ST fusion as a constrained optimization problem consisting of TGTv and TGEc, and developed an efficient algorithm based on P-PDS with OVDp. Experimental results demonstrate that TSSTF performs comparably to state-of-the-art ST fusion methods under noise-free conditions and outperforms them under noisy conditions. In addition, we provided a set of recommended parameter values and confirmed that these settings yield high performance consistently across a variety of target sites and noise conditions. This parameter design enhances the reproducibility and practical utility of TSSTF in real-world applications. TSSTF is expected to have a significant impact on the field of remote sensing by enabling more accurate and reliable estimation of satellite images with high spatial and temporal resolution, even under challenging measurement conditions.

REFERENCES

- [1] M. Zhang, H. Lin, H. Sun, and Y. Cai, "Estimation of vegetation productivity using a Landsat 8 time series in a heavily urbanized area, Central China," *Remote Sens.*, vol. 11, no. 2, p. 133, 2019.
- [2] K. R. Knipper, W. P. Kustas, M. C. Anderson, J. G. Alfieri, J. H. Prueger, C. R. Hain, F. Gao, Y. Yang, L. G. McKee, H. Nieto *et al.*, "Evapotranspiration estimates derived using thermal-based satellite remote sensing and data fusion for irrigation management in California vineyards," *Irrig. Sci.*, vol. 37, no. 3, pp. 431–449, 2019.
- [3] Y. Pan, F. Shen, and X. Wei, "Fusion of Landsat-8/OLI and GOCI data for hourly mapping of suspended particulate matter at high spatial resolution: A case study in the Yangtze (Changjiang) Estuary," *Remote Sens.*, vol. 10, no. 2, p. 158, 2018.
- [4] X. Yang and C. P. Lo, "Using a time series of satellite imagery to detect land use and land cover changes in the Atlanta, Georgia metropolitan area," *Int. J. Remote Sens.*, vol. 23, no. 9, pp. 1775–1798, 2002.
- [5] V. Heimhuber, M. G. Tulbure, and M. Broich, "Addressing spatio-temporal resolution constraints in Landsat and MODIS-based mapping of large-scale floodplain inundation dynamics," *Remote Sens. Environ.*, vol. 211, pp. 307–320, 2018.
- [6] N. J. Pastick, B. K. Wylie, and Z. Wu, "Spatiotemporal analysis of Landsat-8 and Sentinel-2 data to support monitoring of dryland ecosystems," *Remote Sens.*, vol. 10, no. 5, p. 791, 2018.
- [7] M. Chiesi, P. Battista, L. Fibbi, L. Gardin, M. Pieri, B. Rapi, M. Romani, F. Sabatini, and F. Maselli, "Spatio-temporal fusion of NDVI data for simulating soil water content in heterogeneous Mediterranean areas," *Eur. J. Remote Sens.*, vol. 52, no. 1, pp. 88–95, 2019.
- [8] X. Li, Y. Zhou, G. R. Asrar, J. Mao, X. Li, and W. Li, "Response of vegetation phenology to urbanization in the conterminous United States," *Glob. Change Biol.*, vol. 23, no. 7, pp. 2818–2830, 2017.
- [9] F. Gao, J. Masek, M. Schwaller, and F. Hall, "On the blending of the Landsat and MODIS surface reflectance: Predicting daily Landsat surface reflectance," *IEEE Trans. Geosci. Remote Sens.*, vol. 44, no. 8, pp. 2207–2218, 2006.
- [10] X. Zhu, F. Cai, J. Tian, and T. K.-A. Williams, "Spatiotemporal fusion of multisource remote sensing data: Literature survey, taxonomy, principles, applications, and future directions," *Remote Sens.*, vol. 10, no. 4, p. 527, 2018.
- [11] Y. Chen, S. Liu, and X. Wang, "Learning continuous image representation with local implicit image function," in *Proc. IEEE Conf. Comput. Vis. Pattern Recognit. (CVPR)*, 2021, pp. 8628–8638.
- [12] X. Hu, H. Mu, X. Zhang, Z. Wang, T. Tan, and J. Sun, "Meta-SR: A magnification-arbitrary network for super-resolution," in *Proc. IEEE Conf. Comput. Vis. Pattern Recognit. (CVPR)*, 2019, pp. 1575–1584.
- [13] T. Celik, "Unsupervised change detection in satellite images using

- principal component analysis and k -means clustering," *IEEE Geosci. Remote Sens. Lett.*, vol. 6, no. 4, pp. 772–776, 2009.
- [14] S. Takemoto, K. Naganuma, and S. Ono, "Graph spatio-spectral total variation model for hyperspectral image denoising," *IEEE Geosci. Remote Sens. Lett.*, vol. 19, pp. 1–5, 2022.
 - [15] X. Zhu, J. Chen, F. Gao, X. Chen, and J. G. Masek, "An enhanced spatial and temporal adaptive reflectance fusion model for complex heterogeneous regions," *Remote Sens. Environ.*, vol. 114, no. 11, pp. 2610–2623, 2010.
 - [16] X. Zhu, E. H. Helmer, F. Gao, D. Liu, J. Chen, and M. A. Lefsky, "A flexible spatiotemporal method for fusing satellite images with different resolutions," *Remote Sens. Environ.*, vol. 172, pp. 165–177, 2016.
 - [17] Q. Wang, Y. Tang, X. Tong, and P. M. Atkinson, "Virtual image pair-based spatio-temporal fusion," *Remote Sens. Environ.*, vol. 249, p. 112009, 2020.
 - [18] B. Zhukov, D. Oertel, F. Lanzl, and G. Reinhackel, "Unmixing-based multisensor multiresolution image fusion," *IEEE Trans. Geosci. Remote Sens.*, vol. 37, no. 3, pp. 1212–1226, 1999.
 - [19] R. Zurita-Milla, J. G. Clevers, and M. E. Schaepman, "Unmixing-based Landsat TM and MERIS FR data fusion," *IEEE Geosci. Remote Sens. Lett.*, vol. 5, no. 3, pp. 453–457, 2008.
 - [20] Y. Ke, J. Im, S. Park, and H. Gong, "Downscaling of MODIS one kilometer evapotranspiration using Landsat-8 data and machine learning approaches," *Remote Sens.*, vol. 8, no. 3, p. 215, 2016.
 - [21] H. Song, Q. Liu, G. Wang, R. Hang, and B. Huang, "Spatiotemporal satellite image fusion using deep convolutional neural networks," *IEEE J. Sel. Top. Appl. Earth Obs. Remote Sens.*, vol. 11, no. 3, pp. 821–829, 2018.
 - [22] V. Moosavi, A. Talebi, M. H. Mokhtari, S. R. F. Shamsi, and Y. Niazi, "A wavelet-artificial intelligence fusion approach (WAIFA) for blending Landsat and MODIS surface temperature," *Remote Sens. Environ.*, vol. 169, pp. 243–254, 2015.
 - [23] X. Liu, C. Deng, S. Wang, G.-B. Huang, B. Zhao, and P. Lauren, "Fast and accurate spatiotemporal fusion based upon extreme learning machine," *IEEE Geosci. Remote Sens. Lett.*, vol. 13, no. 12, pp. 2039–2043, 2016.
 - [24] Z. Tan, M. Gao, J. Yuan, L. Jiang, and H. Duan, "A robust model for MODIS and Landsat image fusion considering input noise," *IEEE Trans. Geosci. Remote Sens.*, vol. 60, pp. 1–17, 2022.
 - [25] Z. Tan, M. Gao, X. Li, and L. Jiang, "A flexible reference-insensitive spatiotemporal fusion model for remote sensing images using conditional generative adversarial network," *IEEE Trans. Geosci. Remote Sens.*, vol. 60, pp. 1–13, 2021.
 - [26] Q. Liu, X. Meng, X. Li, and F. Shao, "Detail injection-based spatiotemporal fusion for remote sensing images with land cover changes," *IEEE Trans. Geosci. Remote Sens.*, vol. 61, pp. 1–14, 2023.
 - [27] G. Chen, P. Jiao, Q. Hu, L. Xiao, and Z. Ye, "SwinSTFM: Remote sensing spatiotemporal fusion using Swin transformer," *IEEE Trans. Geosci. Remote Sens.*, vol. 60, pp. 1–18, 2022.
 - [28] B. Huang and H. Song, "Spatiotemporal reflectance fusion via sparse representation," *IEEE Trans. Geosci. Remote Sens.*, vol. 50, no. 10, pp. 3707–3716, 2012.
 - [29] S. Chen, J. Wang, and P. Gong, "ROBOT: A spatiotemporal fusion model toward seamless data cube for global remote sensing applications," *Remote Sens. Environ.*, vol. 294, p. 113616, 2023.
 - [30] R. Isono, K. Naganuma, and S. Ono, "Robust spatiotemporal fusion of satellite images: A constrained convex optimization approach," *IEEE Trans. Geosci. Remote Sens.*, vol. 62, pp. 1–16, 2024.
 - [31] J. Xue, Y. Leung, and T. Fung, "A Bayesian data fusion approach to spatio-temporal fusion of remotely sensed images," *Remote Sens.*, vol. 9, no. 12, p. 1310, 2017.
 - [32] A. Li, Y. Bo, Y. Zhu, P. Guo, J. Bi, and Y. He, "Blending multi-resolution satellite sea surface temperature (SST) products using Bayesian maximum entropy method," *Remote Sens. Environ.*, vol. 135, pp. 52–63, 2013.
 - [33] L. I. Rudin, S. Osher, and E. Fatemi, "Nonlinear total variation based noise removal algorithms," *Physica D*, vol. 60, no. 1–4, pp. 259–268, 1992.
 - [34] X. Bresson and T. F. Chan, "Fast dual minimization of the vectorial total variation norm and applications to color image processing," *Inverse Probl. Imaging (Springfield)*, vol. 2, no. 4, pp. 455–484, 2008.
 - [35] Q. Yuan, L. Zhang, and H. Shen, "Hyperspectral image denoising employing a spectral-spatial adaptive total variation model," *IEEE Trans. Geosci. Remote Sens.*, vol. 50, no. 10, pp. 3660–3677, 2012.
 - [36] T. Pock and A. Chambolle, "Diagonal preconditioning for first order primal-dual algorithms in convex optimization," in *Proc. IEEE Int. Conf. Comput. Vis. (ICCV)*, 2011, pp. 1762–1769.
 - [37] M. V. Afonso, J. M. Bioucas-Dias, and M. A. Figueiredo, "An augmented Lagrangian approach to the constrained optimization formulation of imaging inverse problems," *IEEE Trans. Image Process.*, vol. 20, no. 3, pp. 681–695, 2010.
 - [38] G. Chierchia, N. Pustelnik, J.-C. Pesquet, and B. Pesquet-Popescu, "Epigraphical projection and proximal tools for solving constrained convex optimization problems," *Signal, Image Video Process.*, vol. 9, no. 8, pp. 1737–1749, 2015.
 - [39] S. Ono and I. Yamada, "Signal recovery with certain involved convex data-fidelity constraints," *IEEE Trans. Signal Process.*, vol. 63, no. 22, pp. 6149–6163, 2015.
 - [40] S. Ono, "Primal-dual plug-and-play image restoration," *IEEE Signal Process. Lett.*, vol. 24, no. 8, pp. 1108–1112, 2017.
 - [41] S. Ono, "L₀ Gradient Projection," *IEEE Trans. Image Process.*, vol. 26, no. 4, pp. 1554–1564, 2017.
 - [42] K. Naganuma and S. Ono, "Variable-wise diagonal preconditioning for primal-dual splitting: Design and applications," *IEEE Trans. Signal Process.*, pp. 1–15, 2023.
 - [43] A. Chambolle and T. Pock, "A first-order primal-dual algorithm for convex problems with applications to imaging," *J. Math. Imaging Vis.*, vol. 40, no. 1, pp. 120–145, 2011.
 - [44] R. Isono and S. Ono, "Temporally-guided total variation for robust spatiotemporal fusion of satellite images," in *Proc. IEEE Int. Conf. Acoust., Speech, Signal Process. (ICASSP)*, 2024, pp. 2520–2524.
 - [45] P. L. Combettes and N. N. Reyes, "Moreau's decomposition in Banach spaces," *Math. Program.*, vol. 139, no. 1–2, pp. 103–114, 2013.
 - [46] L. Condat, "Fast projection onto the simplex and the l1 ball," *Math. Program.*, vol. 158, no. 1–2, pp. 575–585, 2016.
 - [47] H. Song and B. Huang, "Spatiotemporal satellite image fusion through one-pair image learning," *IEEE Trans. Geosci. Remote Sens.*, vol. 51, no. 4, pp. 1883–1896, 2012.
 - [48] J. Farrell, F. Xiao, and S. Kavusi, "Resolution and light sensitivity tradeoff with pixel size," in *Proc. SPIE Electronic Imaging*, vol. 6069, 2006, p. 211–218.
 - [49] S. C. Park, M. K. Park, and M. G. Kang, "Super-resolution image reconstruction: a technical overview," *IEEE Signal Process. Mag.*, vol. 20, no. 3, pp. 21–36, 2003.
 - [50] N. Yokoya, T. Yairi, and A. Iwasaki, "Coupled nonnegative matrix factorization unmixing for hyperspectral and multispectral data fusion," *IEEE Trans. Geosci. Remote Sens.*, vol. 50, no. 2, pp. 528–537, 2011.
 - [51] H. Shen, X. Meng, and L. Zhang, "An integrated framework for the spatio-temporal-spectral fusion of remote sensing images," *IEEE Trans. Geosci. Remote Sens.*, vol. 54, no. 12, pp. 7135–7148, 2016.
 - [52] I. V. Emelyanova, T. R. McVicar, T. G. Van Niel, L. T. Li, and A. I. Van Dijk, "Assessing the accuracy of blending Landsat–MODIS surface reflectances in two landscapes with contrasting spatial and temporal dynamics: A framework for algorithm selection," *Remote Sens. Environ.*, vol. 133, pp. 193–209, 2013.
 - [53] J. Li, Y. Li, L. He, J. Chen, and A. Plaza, "Spatio-temporal fusion for remote sensing data: An overview and new benchmark," *Sci. China Inf. Sci.*, vol. 63, no. 4, pp. 1–17, 2020.
 - [54] D. Guo, W. Shi, H. Zhang, and M. Hao, "A flexible object-level processing strategy to enhance the weight function-based spatiotemporal fusion method," *IEEE Trans. Geosci. Remote Sens.*, vol. 60, pp. 1–11, 2022.
 - [55] Z. Wang, A. C. Bovik, H. R. Sheikh, and E. P. Simoncelli, "Image quality assessment: from error visibility to structural similarity," *IEEE Trans. Image Process.*, vol. 13, no. 4, pp. 600–612, 2004.



Ryosuke Isono (S'23) received B.E. and M.E. degrees in Information and Computer Science in 2022 from the Osaka University and from the Tokyo Institute of Technology, respectively. He is currently pursuing a Ph.D. degree with the Department of Computer Science at the Institute of Science Tokyo. His current research interests include signal and image processing, mathematical optimization, and remote sensing.



Shunsuke Ono (S'11–M'15–SM'23) received a B.E. degree in Computer Science in 2010 and M.E. and Ph.D. degrees in Communications and Computer Engineering in 2012 and 2014 from the Tokyo Institute of Technology, respectively. From 2012 to 2014, he was a Research Fellow (DC1) of the Japan Society for the Promotion of Science (JSPS). He was an Assistant, then an Associate Professor with Tokyo Institute of Technology (TokyoTech), Tokyo, Japan, from 2014 to 2024. From 2016 to 2020, he was a Researcher of Precursory Research for Embryonic

Science and Technology (PRESTO), Japan Science and Technology Agency (JST), Tokyo, Japan. Currently, he is an Associate Professor with Institute of Science Tokyo (Science Tokyo), Tokyo, Japan. His research interests include signal processing, image analysis, optimization, remote sensing, and measurement informatics. He has served as an Associate Editor for IEEE TRANSACTIONS ON SIGNAL AND INFORMATION PROCESSING OVER NETWORKS (2019–2024). Dr. Ono was a recipient of the Young Researchers' Award and the Excellent Paper Award from the IEICE in 2013 and 2014, respectively, the Outstanding Student Journal Paper Award and the Young Author Best Paper Award from the IEEE SPS Japan Chapter in 2014 and 2020, respectively, and the Best Paper Award in APSIPA ASC 2024. He also received the Funai Research Award in 2017, the Ando Incentive Prize in 2021, the MEXT Young Scientists' Award in 2022, and the IEEE SPS Outstanding Editorial Board Member Award in 2023.